Theses and Dissertations | Graduate School

2019

Optimizing Gas Mixture Composition for the RTPC Detector for BONuS 12 at Jefferson Lab.

joshua h. lehman

Optimizing Gas Mixture Composition for the RTPC Detector for BONuS 12 at Jefferson Lab.

Thesis by
Joshua Harvey Lehman

In Partial Fulfillment of the Requirements for the
Degree of
Masters of Physics

VIRGINIA COMMONWEALTH UNIVERSITY

Richmond, Virginia

2019

Defended [04, 2019]

© 2019

Joshua Harvey Lehman
ORCID: xxxxx

ACKNOWLEDGEMENTS

Dedicated to my son Gavin Lehman. If it were not for him, I would not be here today. Gavin, you saved my life and I hope that I make you proud. I love you little man . . . Dad

ABSTRACT

The main objective of this thesis is to perform a study of and optimize the most direct and practical gas mixture composition inside the Radial Time Projection Chamber for the Barely-Offshell Nucleon Structure (BONuS 12) detector for use in the CLAS 12 detector in Experimental Hall B at Thomas Jefferson National Accelerator Facility (JLab). The optimization of these conditions will enhance the performance and resolution of the detector. The original BONuS 6 experiment utilized a gas composition of 80 % He and 20% Dimethyl Ether (DME). With the extensive 12 GeV energy upgrade constructed at JLab and the new BONuS 12 detector established , it is imperative that the gas composition utilized, is best suited to facilitate the experimental needs and demands. BONuS 12 is an experiment designed to measure the momentum of recoiling spectator protons down to 70 MeV/c. This technique will extract the structure function F_2^n at large x from 0.1 up to 0.8 over a significant range in Q^2 and W from the nucleon mass, with a beam energy of 11 GeV, enabling us to essentially select free neutrons.

TABLE OF CONTENTS

LIST OF ILLUSTRATIONS

LIST OF TABLES

Chapter 1

INTRODUCTION

1.1 Introduction

Three Generations
of Matter (Fermions)

	I	II	III	
mass→	2.4 MeV	1.27 GeV	171.2 GeV	0
charge→	⅔	⅔	⅔	0
spin→	½ **u**	½ **c**	½ **t**	1 **γ**
name→	up	charm	top	photon
	4.8 MeV	104 MeV	4.2 GeV	0
	-⅓	-⅓	-⅓	0
	½ **d**	½ **s**	½ **b**	1 **g**
	down	strange	bottom	gluon
	< 2.2 eV	< 0.17 MeV	< 15.5 MeV	91.2 GeV
	0	0	0	0
	½ **V**$_e$	½ **V**$_\mu$	½ **V**$_\tau$	1 **Z**^{0}
	electron neutrino	muon neutrino	tau neutrino	weak force
	0.511 MeV	105.7 MeV	1.777 GeV	80.4 GeV
	-1	-1	-1	±1
	½ **e**	½ **μ**	½ **τ**	1 **W**$^\pm$
	electron	muon	tau	weak force

Quarks / Leptons / Bosons (Forces)

Figure 1.1: The Standard Model

It is a well known fact that all matter is composed of atoms and that these atoms are composed of a central nucleus with electrons that move around it. The nucleus is composed of nucleons, which is a name for the protons and neutrons. Since James Chadwick discovered the neutron in 1932, protons and neutrons were thought to be the smallest indivisible elemental particles. This thought of matter held until the 1960s. As research progressed so did our understanding of nucleons. Since then, more and more evidence showed that protons and neutrons had internal structure. We have now come to learn that protons and neutrons are composted of quarks, where the proton is a combination of two up quarks and one down quark and the

neutron is composed of one up quark and two down quarks. We are able to study partonic structure of the proton via high-energy lepton-nucleon scattering or, in other words, through Deep Inelastic Scattering (DIs) and examining the structure functions. The structure function is essentially a probability density function.

The ordinary electrons, up-quarks, and down-quarks found in atoms today are relics of a high energy explosion at the beginning of time [22]. Particle physics (high energy physics) focuses on relativistic transformations of energy that reveal the extraordinary particles and fields. These particles include the muon μ^- and τ^- (heavy electrons), the neutrinos ν_e, ν_μ, and ν_τ (neutral electron like particles), the c(charm), s(strange), t(top), b(bottom) quarks, the vector bosons $W^\pm$ and Z (analogous to photons) which mediate the weak interactions, and eight bi-colored gluons which are the quanta of the color force [22]. Every particle is found to have an antiparticle of opposite charge but identical mass associated with it. When it comes to the standard model, matter and antimatter are generally created and destroyed together.

In an effort to categorize all of these particles and their interactions in a coherent fashion, physicists have developed the standard model, as seen in Fig 3.1. This model describes three of the four known fundamental forces of nature. These forces are the electromagnetic force, the weak force, and the strong force. The standard model is our best understanding of how these particles and three of the forces interact. Developed in the early 1970's, it has been able to explain experimental results and accurately predicts a vast area of phenomena.

As the early universe expanded and cooled, vast numbers of particle-antiparticle pairs annihilated to photons leaving the relative small excess of matter (about one baryon per 10^9 photons) seen today [22]. In 1964, the constituent quark model (CQM) was proposed by Gell-Mann and Zweig in order to explain particles and their strong interactions in the language of quarks [2]. In the CQM model, particles made up of quarks can fall into one of two groups: mesons and baryons. Mesons are composed of quark and anti-quark pairs, where baryons are composed of three quarks. Mesons and baryons are labeled together to form the family of hadrons. The quantum numbers of a hadron can be formed by considering the quark components, which can be

Symbol	Name	Mass (GeV/c^2)	Charge (e)	Isospin
d	Down	0.0015-0.005	-1/3	1/2
u	Up	0.003-0.009	2/3	1/2
s	Strange	0.06-0.17	-1/3	0
c	Charm	1.1-1.4	2/3	0
b	Bottom	4.1-4.4	-1/3	0
t	Top	168.6-179.0	2/3	0

Table 1.1: Quarks and their properties

seen in Table 1.1. This model was able to explain most hadrons, however it violated Fermi-Dirac statistics, which were postulated by Fermi in 1952, when the attempt was made to describe the Δ^{++} hadron. This hadron has spin 3/2 and charge +2, and is interpreted as a *uuu* bound state with zero orbital angular momentum and three parallel spins. In the case of the Δ^{++} hadron, the wave function is completely symmetric which violates the Pauli exclusionary principle. In order to deal with this, a new quantum number with three possible states which can change from one to another was introduced [3]. This quantum number was later named "color", and the three states are categorized as red, green, and blue. This "color charge" provides an additional gauge degree of freedom to the CQM . It was later realized that quarks and gluons couple to the color charge in a theory known as Quantum Chromodynamics (QCD). There are two main properties of QCD, asymptotic freedom and confinement. Asymptotic freedom tells us that in very high energy reactions, quarks and gluons interact very weakly and if the quarks are close enough to each other, the strong interaction between them is so weak that they behave as if they were free particles [4]. Confinement means that the force between the quarks increases as the distance between them is increased. Due to this, it would take an infinite amount of energy to separate the two quarks. Although this phenomenon has not been shown analytically, it seems to hold true because it can explain the consistent failure to find a free quark existing by itself.

The nucleon can also be described by the wavefunctions of its constituents. From quantum field theory, we know that the quarks and gluons inside of hadrons can have several kinds of interactions. Gluons can split into quark-antiquark pairs that can interact with the other valence or sea quarks or radiate gluons [3]. This amount of complexity of hadrons calls for specific

tools and jargon to describe its structure in logical ways. One of the primary methods we have at our disposal to describe and investigate this complex structure is electron scattering. The formalism presented in this chapter follows that of Refs [2] and [3].

The structure of nucleons and their excited states, known as resonances, is an active area of experimental particle physics. A widely adopted method of probing the internal structure of nucleons is done through electron scattering. Large efforts has been made to obtain accurate measurements of the inclusive electron cross section. Typically in an experiment, only the momentum of the scattered electron is recorded. What is actually measured is the aforementioned "inclusive" cross section, in which all final states X, and all possible outgoing momenta are included. At special energies where the particles involved "like" to interact and form short-lived semibound state before breaking apart. The nucleon resonances are wide and overlapping, so inclusive measurements are not capable of distinguishing and studying every one of them. More data can be attained by measuring the other outgoing particles together with the scattered electron. These measurements are known as "exclusive" because the final state of the reaction is completely determined.

1.2 Physics Motivation

The physics motivation section will take the form of Ref [19]. Most of our information on the structure of the nucleon ranging from its elastic for factors, to its deep inelastic structure functions, comes from many decades of experiments on proton targets. A complete determination of the valence content of the nucleon can be achieved only when both its up and down quark distributions are known. This requires charged lepton scattering from the neutron. In principle, the valence up and down quark distributions can be separated via neutrino and antineutrino scattering on the proton. However, to date there have been no measurements performed with the requisite precision to adequately constrain the down quark distribution at large values of x.

The absence of free neutron targets has meant that the traditional method for extracting neutron structure information has been to use deuterium targets, and apply nuclear corrections arising from the Fermi motion and bind-

ing of the nucleons in the deuteron. while this is sufficient in some cases, for many neutron observables, especially ones sensitive to the high momentum components of the deuteron wave function, the nuclear model uncertainties can be fairly large. As a result, our knowledge of the structure of the neutron, especially in the deep inelastic region at large x, is inadequate. The x term as mentioned before is the fraction of the nucleon's momentum that is carried by the struck quark. Given the extremely high quality of proton data that is being accumulated at Jefferson Lab and other facilities, obtaining a similar level of accuracy for the structure of the free neutron is a high priority.

In this section I highlight several examples which would benefit dramatically from a more accurate determination of the structure of the free neutron. We focus on the ratio of down to up quark distributions at large x, which currently has very large (over 50 to 100 percent, depending on the nuclear corrections models used) uncertainties for $x > 0.6$. Some other quantities which will be able to be measured with the BoNuS12 experiment (but not mentioned in this thesis) include the elastic neutron form factor,quark-hadron duality, large-x parton distribution functions, semi-inclusive DIS channels, hard exclusive reactions such as deeply-virtual Compton scattering or deeply-virtual meson production, as well as the inclusive structure function of a virtual pion.

Finally, we note that the data could provide an important testing ground for calculations of various nuclear effects in the deuteron. In addition to isolating the kinematics of the recoil proton where these effects are small, the data will also provide coverage into kinematic regions where particular effects, such as dynamical off-shell effects, are expected to become significant.

1.3 Kinematics of Electron Scattering

A detailed picture of the nucleon can be formulated by measuring the four-momentum of electrons which have been scattered after exchanging a virtual photon with the nucleon. The resolution of this photograph is determined by the momentum of the exchanged boson. Higher exchanged momentum corresponds to smaller wavelength of the probe, giving access to smaller structures within the larger object. Fig 1.2 depicts the lowest order (Born) approximation of the inclusive lepton-nucleon interaction.

In this figure, the electron comes in with an initial energy, E, initial four-momentum (E, k) and goes out with final four-momentum (E', k') and with an angle θ_e with respect to the incident direction. A virtual photon is emitted that interacts with a target nucleon N at rest, whose four-momentum is given by $N(M, O)$. Where four-momentum is similar to three-momentum, except it contains four components. In other words, four-momentum contains the familiar components of momentum and the fourth component in the time direction. This fourth component turns out to be proportional to the energy of the system. A virtual photon is a transient fluctuation that acts as an ordinary photon but whose lifetime is limited by the uncertainty principle. The energy transferred from the lepton to the nucleon is equal to the energy of the virtual photon γ^*, and is denoted in Lorentz invariant form by Eq.1.1.

$$\nu = \frac{p \cdot q}{M} \tag{1.1}$$

Where p is the four-momentum of the struck nucleon, q is the four-momentum of the virtual photon and M is the nucleons mass. It can be shown that the energy transfer in the labframe is $\nu = E - E'$. The degree of virtuality is $q^2 = \nu^2 - q^2$ and we make the definition

$$Q^2 \equiv q^2 \approx 4EE' sin^2(\frac{\theta}{2}) \tag{1.2}$$

The quantity Q^2 is a measure of the virtual photon's wavelength. The invariant mass squared of the recoiling hadronic system (X in Fig.1.2)is related to Q^2 and ν by,

$$W^2 = (p + q)^2 = M^2 + 2M\nu - Q^2 \tag{1.3}$$

When the incident electron excites the nucleon into a resonance state, W is the mass of the excited resonance. Below $W = 2.0 GeV$, the so-called resonance region, is characterized by clear peaks, when scattering from a free nucleon. Two more useful Lorentz invariants are the dimensionless Bjorken scaling variable, x(more on the interpretation of this quantity is given in the next section), and the fraction of the beam energy carried by the virtual photon, y, which are given by
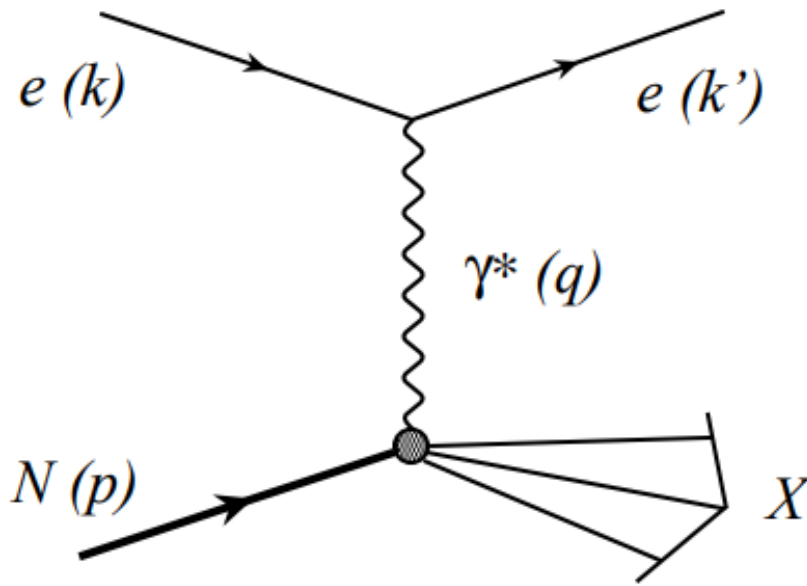
Figure 1.2: The kinematics of inclusive lepton-nucleon scattering in the Born approximation

(one photon exchange). The four-momenta of the electrons(e), the virtual photon (γ^*) and the nucleon target (N) are given in parenthesis.

$$x = \frac{Q^2}{2p \cdot q} = \frac{Q^2}{2M\nu}, \qquad (1.4)$$

$$y = \frac{p \cdot q}{p \cdot k} = \frac{\nu}{E}. \qquad (1.5)$$

We can write Eq. 1.3 in terms of x, $W^2 = M^2 + Q^2(1-x)/x$ and see that for the special case of elastic scattering (when $W = M$) that $x = 1$ and $Q^2 = 2M\nu$

1.4 Deep Inelastic Scattering

Traditionally, $Q^2 > 1.0 GeV^2$ and $W > 2.0 GeV$ defines the deep inelastic scattering (DIS) region. Here, no more discernable resonance peaks exist because the number of resonances per unit energy and their widths increase to a level where they can no longer be separated. Also, the virtual photon resolution is sufficient to scatter incoherently from individual quarks in the nucleon. Thus, the large momentum transfer enables us to directly probe the substructure of the nucleon.

We can express the doubly-differential cross section for scatter unpolarized leptons from unpolarized nucleon targets as

$$\frac{d^2\sigma}{d\Omega dE'} = \frac{\alpha^2}{Q^4}\frac{E'}{E}L_{\mu\nu}W^{\mu\nu},$$

(1.6)

Where α is the fine-structure constant, $d\Omega$ is the solid angle into which the lepton is scattered in the lab frame, and $L_{\mu\nu}$ and $W^{\mu\nu}$ are the leptonic and hadronic tensors, respectively. When summed and averaged over spins, the leptonic tensor can be written as

$$L_{\mu\nu} = 2(k_\mu k'_\nu + k'_\nu k_\nu - g_{\mu\nu}k \cdot k')$$

(1.7)

and can be directly calculated from the rules of Quantum Electrodynamics (QED). The hadronic tensor, on the other hand, is a general way of parameterizing a complex system that we cannot calculate from first principles. Anti-symmetric contribution to this term cancel out in the contraction with the leptonic tensor so we can write $W^{\mu\nu}$ containing two independent structures

$$W^{\mu\nu} = W_1(\nu, Q^2)(\frac{q^{mu}q^\nu}{q^2} - g^{\mu\nu}) + \frac{W_2(\nu, Q^2)}{M^2}(p^\nu + \frac{p \cdot q}{q^2}q^\mu)(p^\nu + \frac{p \cdot q}{q^2}q^\nu)$$

(1.8)

where W_1 and W_2 are inelastic structure functions of the Lorentz scalar variables q^2 and ν that parameterize our ignorance of nucleon structure. We can now contract the tensors in Eqs. 1.7 and 1.8 and combine with Eq. 1.6 to find the following form for the cross section:

$$\frac{d^2\sigma}{d\Omega dE'} = \sigma_{Mott}(2W_1(\nu, Q^2)tan^2(\frac{\theta}{2}) + W_2(\nu, Q^2). \tag{1.9}$$

The Mott cross section, σ_{Mott}, describes relativistic electron scattering from a spinless point particle in a Coulomb field,

$$\sigma_{Mott} = \frac{4\alpha^2 E'^2}{Q^4}cos^2(\frac{\theta}{2}). \tag{1.10}$$

Two independent structure function exist in Eq 1.9 because the total photoabsorption cross section can be split into independent portions, transverse (helicity $\lambda = \pm 1$) and longitudinal ($\lambda = 0$). If we take the virtual photon as moving along the z-axis it has polarization vectors,

$$\lambda = \pm 1 : \epsilon_\pm = \mp\sqrt{\frac{1}{2}}(0; 1, \pm i, 0), \tag{1.11}$$

$$\lambda = 0 : \epsilon_0 = \frac{1}{\sqrt{Q^2}}(\sqrt{Q^2 + \nu^2}; 0, 0, \nu). \tag{1.12}$$

and the total cross sections for the interaction of polarized photons on unpolarized nucleons becomes

$$\sigma_\lambda^{tot} = \frac{4\pi^2\alpha}{K}\epsilon_\lambda^{\mu*}\epsilon_\lambda^\nu W_{\mu\nu}, \tag{1.13}$$

where K is the incident flux of photons. Since we are dealing with the virtual photon case ($Q^2 \neq 0$), K is somewhat arbitrary and we choose the Hand convention to make our definition take the form of the following

$$K = \frac{W^2 - M^2}{2M}\nu(1 - x) \tag{1.14}$$

Now the differential cross section can be expressed in term of σ_T and σ_L, the transverse and longitudinal cross sections become

$$\sigma \equiv \frac{d^2\sigma}{d\Omega dE'} = \Gamma(\sigma_T + \epsilon\sigma_L \tag{1.15}$$

Where Γ is the flux of transverse virtual photons,

$$\Gamma = \frac{\alpha}{2\pi^2 Q^2} \frac{E'}{E} \frac{K}{1 - \epsilon} \tag{1.16}$$

and the ratio of virtual photon polarizations are given be

$$\epsilon = [1 + 2(1 + \frac{\nu^2}{Q^2})tan^2(\frac{\theta}{2})]^{-1}. \tag{1.17}$$

The components of the total virtual photoabsorption cross section can be found by contracting the polarization vectors of Eqs 1.11 and 1.12 with $W^{\mu\neq}$ from Eq. 1.8

$$\sigma_T \equiv \frac{1}{2}(\sigma_+^{tot} + \sigma_-^{tot}) = \frac{4\pi^2\alpha}{K} W_1(\nu, Q^2) \tag{1.18}$$

$$\sigma_L \equiv \sigma_0^{tot} = \frac{4\pi^2\alpha}{K}[(1 + \frac{\nu^2}{Q^2})W_2(\nu, Q^2) + W_1(\nu, Q^2)]. \tag{1.19}$$

Finally, the photon polarization cross section ration, R, turns out to be a useful quantity,

$$R \equiv \frac{\sigma_L}{\sigma_T} = \frac{W_2}{W_1}(1 + \frac{\nu^2}{Q^2}) - 1. \tag{1.20}$$

1.5 The Quark-Parton Model

We know that W_1 and W_2 are scalar functions of ν and Q^2 [3] but Bjorken predicted that in the deep inelastic regime the structure function would be independent of ν and Q^2 but dependent on the ratio, x, the famous scaling variable which carries Bjorken's name

$$MW_1(\nu, Q^2) \to F_1(x); Q^2 \to \infty, \nu \to \infty; \nu W_2(\nu, Q^2) \to F_2(x) \qquad (1.21)$$
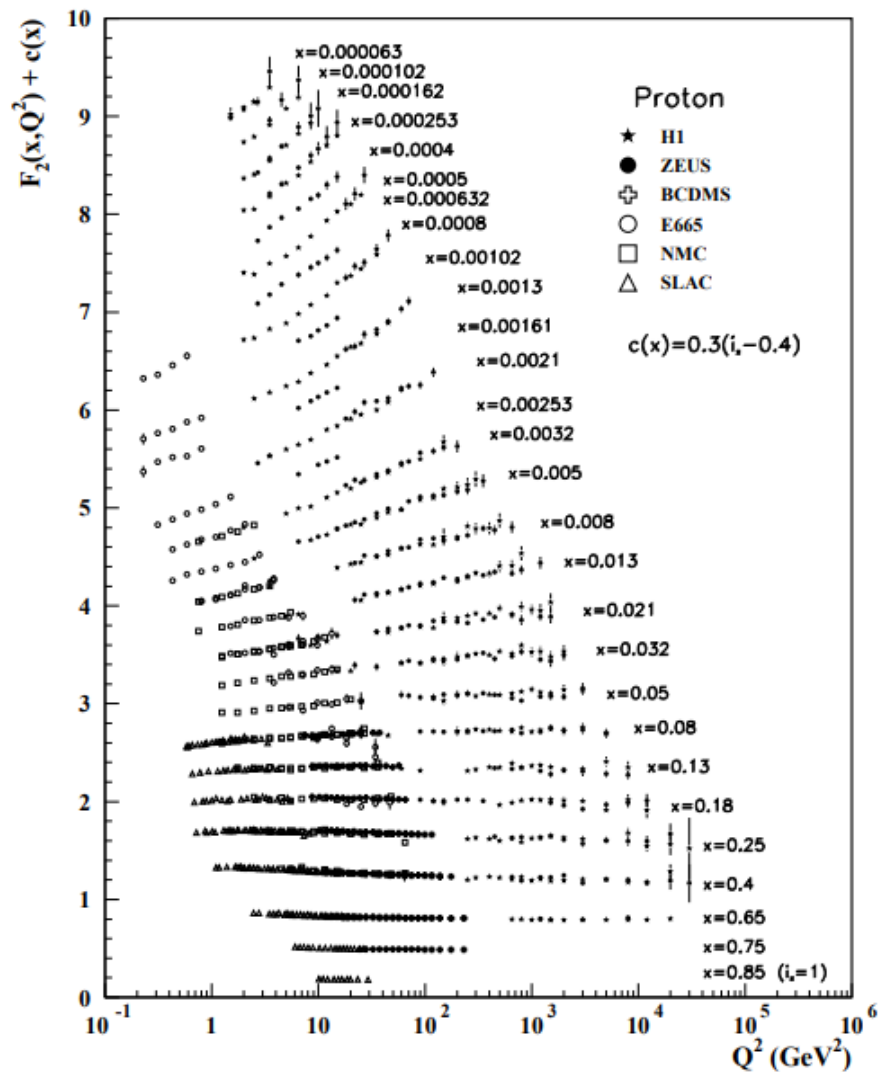
Figure 1.3: The Particle Data Group Compilation of the protons structure function

F_2 plus an x dependent offset to visually separate the data [3].

Fig 1.3 depicts how, at moderate x, F_2^p is independent of W^2 over four orders of magnitude, leading to the conclusion that inelastic electron-proton scattering is equivalent to incoherent elastic scatter from point-like "partons" within the nucleon. QCD scaling violations (F_2 increasing with Q^2 at very low x and decreasing with Q^2 at high x) do occur and are described with QCD.

The Quark-Parton Model (QPM) was originally formulated by Feynman, Bjorken, and Paschos [3] to describe the early deep inelastic scattering data. The structure functions are Lorentz invariants and therefore remain unchanged under a boost to the infinite-momentum frame ($|p| \rightarrow \infty$). In this frame the interaction between the substructure of partons is a direct analogy with the nuclear impulse approximation. In other words, the electron interacts so quickly with one parton that the other do not have time to react. Them model also makes the assumption that the partons have no internal electromagnetic structure and have a negligible mass in the Bjorken limit ($\nu, Q^2 \rightarrow \infty, x\,fixed$). The structure function in the QPM can be written as the sum over quark and antiquark distribution functions

$$F_1(x) = \frac{1}{2} \sum_i e_i^2 f_i(x) \tag{1.22}$$

$$F_2(x) = x \sum_i e_i^2 f_i(x) = 2xF_1(x) \tag{1.23}$$

Where $f_i(x)$ are the Parton Distrubution Functions (PDFs) and can be defined as the probability to find a quark of flabor i, electric charge e_i, and momentum fraction x in the proton. The relationship between F_1 and F_2 in Eq.1.23 is known as the Callan-Gross Relation [3]. The differential cross section from Eq.1.9 can be written in terms of the dimensionless F_1 and F_2 structure functions as

$$\frac{d^2\sigma}{d\Omega dE'} = \sigma_{Mott}(\frac{2}{M}F_1(x, Q^2)tan^2(\frac{\theta}{2}) + \frac{1}{\nu}F_2(x, Q^2)), \tag{1.24}$$

and we can also express the structure functions in terms of σ_T and σ_L

$$F_1(x, Q^2) = \frac{K}{4\pi^2\alpha}M\sigma_T(x, Q^2), \tag{1.25}$$

$$F_2(x, Q^2) = \frac{K}{4\pi^2\alpha} \frac{\nu}{(1 + \frac{\nu^2}{Q^2}} [\sigma_T(x, Q^2) + \sigma_L(x, Q^2)]. \qquad (1.26)$$

The ratio R can also be written in terms of $F_1 4$ and F_2 as

$$R = \frac{F_2}{2xF_1}(1 + \frac{4M^2x^2}{Q^2}) - 1 \qquad (1.27)$$

So we can now see that when we possess knowledge of R and a measurement of differential cross sections can yield an extraction of F_2 from inclusive electron scattering,

$$F_2 = \frac{\sigma}{\sigma_{Mott}}\nu\epsilon\frac{1+R}{1+\epsilon R} \qquad (1.28)$$

where σ is given by Eq.1.15.

1.6 Nucleon Structure at Large x

Although a large body of deep inelastic structure function data exists over a wide range of x and Q^2, the region $x > 0.6$ is not well explored. For $x \geq 0.4$ the contributions from the $q\bar{q}$ sea are negligible, and the structure functions are dominated by the valence quarks. Knowledge of the valence quark distributions of the nucleon at large x is vital for several reasons. The simplest SU(6)symmetric quark model predicts that the ratio of down to up quark distributions in the proton is 1/2; however, the breaking of this symmetry in nature results in a much smaller ratio. Various mechanisms have been invoked to explain why the $d(x)$ distribution is softer than $u(x)$. If the interaction between quarks that are spectators to the deep inelastic collision is dominated by one-gluon exchange, for instance, the down quark distribution will be suppressed, and the d/u ratio will tend to zero in the limit $x \rightarrow 1$. This assumption has been built into most global analyses of parton distribution functions, and has never been tested independently.

On the other hand, if the dominant reaction mechanism involves deep inelastic scattering from a quark with the same spin orientation as the nucleon, as predicted by QCD counting rules, then the effect is to perturb the spin-flavor symmetric wave function such that d/u tends to $\approx 1/5$ as $x \rightarrow 1$. Determining d/u experimentally would therefore lead to important insights into the mechanisms responsible for spin-flavor symmetry breaking.

Because of the 4:1 weighting of the squared quark charges between the up and down quarks, data on the proton structure function, F_2^p, providing strong constraints on the u quark distribution at large x.

$$F_2^n(x) = x \sum_q e_q^2 (q(x) + \bar{q}(x)) \approx x(\frac{4}{9}u(x) + \frac{1}{9}d(x)). \qquad (1.29)$$

Note that for simplicity F_2^p in Eq 1.1 is written to leading order in α_s; where in practice next-to-leading order (NLO) expressions for structure functions are utilized. The determination of the down quark distribution, on the other hand, requires in addition the measurement of the neutron structure function, F_2^n. In particular, the d/u ratio can be determined from the ratio of neutron to proton structure functions,

$$\frac{F_2^n}{F_2^p} \approx \frac{1 + 4d/u}{4 + d/u}, \tag{1.30}$$

provided $x \geq 0.4$ (at moderate to high Q^2) so that the sea quark content can be neglected. These kinematics are ideal for measurements at Jefferson Lab with an 11 GeV electron beam energy.

In the past, data on F_2^n has been primarily from inclusive scattering off deuterium. Unfortunately, theoretical uncertainties in the treatment of nuclear corrections have given yield to ambiguities in the extracted F_2^n at large x. In particular, inclusion of Fermi motion and nucleon off-shell corrections in the deuteron can lead to values for F_2^n / F_2^p which differ by 50 percent already at $x = 0.75$, and varies by a factor of 2-3 at $x = 0.85$. This uncertainty is illustrated in Fig 1.4 which shows F_2^n / F_2^p extracted from the same SLAC data on the proton and deuteron structure functions., with the nuclear corrections estimated on the basis of Fermi motion only (squares), taking nucleon off-shell effects into account and using a model assuming suppression of point-like configurations (PLC) in the spread in the model predictions for the $x \to 1$ behavior, which are indicated by the arrows. The tagged structure function method for measuring F_2^n proposed here virtually eliminates the uncertainties from the nuclear models.
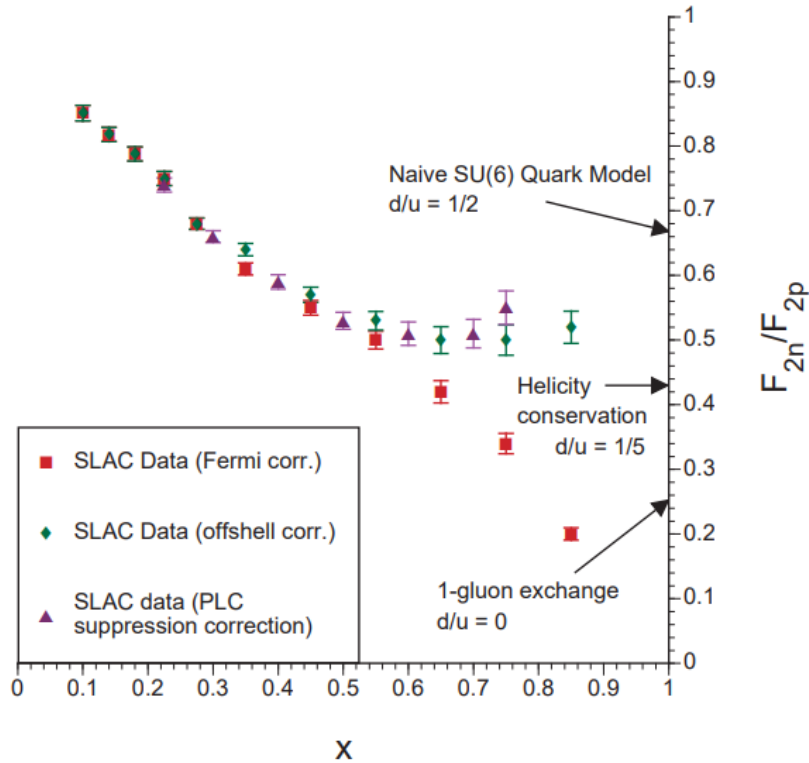
Figure 1.4: Neutron to proton structure function ratio

extracted from SLAC proton and deuteron data [9], assuming different prescriptions for the nuclear corrections, as described in the the text. Several predictions for the $x \to 1$ limits are indicated with arrows.

1.7 Previous BONuS Experiment

In 2005, an experiment was carred out in Hall B of the Thomas Jefferson National Accelerator Facility (TJNAF) called the Barely off-shell Nuclear Structure (BONuS) experiment. Electrons with beam energies of 1.1005, 2.1426, 4.2262 and 5.2681 GeV were used to bombard a gaseous deuterium target. A Radial Time Projection Chamber (RTPC) was built to measure low energy spectator protons to study the $D(e, e'\pi^- p)p$ reaction. With this detector, protons with momentum as low as 67 MeV/c were measured.

The results of this experiment showed the extracted neutron structure function F_2^n and its ratio to the inclusive deuteron structure function F_2^d are presented in both the resonances and the deep-inelastic regions for momentum transfer squared Q^2 between 0.7 and 5 GeV^2/c^2, invariant mass W between 1 and 2.7 GeV/c^2, and Bjorken x between 0.25 and 0.6 (in the deep-inelastic

scattering region). The dependence of the semi-inclusive cross section on the spectator proton momentum and angle was investigated, and tests of the spectator mechanism for different kinematics were preformed. One of the main goals of this experiment was to pin down the behavior of the F_2^n at large x values in the DIS (Deep Inelastic Scattering) region. However, due to the kinematic reach of the BONuS experiment was restricted by the maximum available beam energy of 5.25 GeV/c^2, which limited the experiment to a maximum x value of $x < 0.55$ if $W^* > 2GeV/c^2$ and if $W^* > 1.8GeV/c^2$, this would not extend the values for x beyond $x = 0.6$, which is the region where the uncertainty on the down quark distribution function becomes large. The results were compared over the measured range of $(0.2 < x < 0.65)$ with existing next-to-leading-order fits based on world data. Fig 1.5 shows the results obtained for F_2^n using the Monte-Carlo and the ratio methods [23].
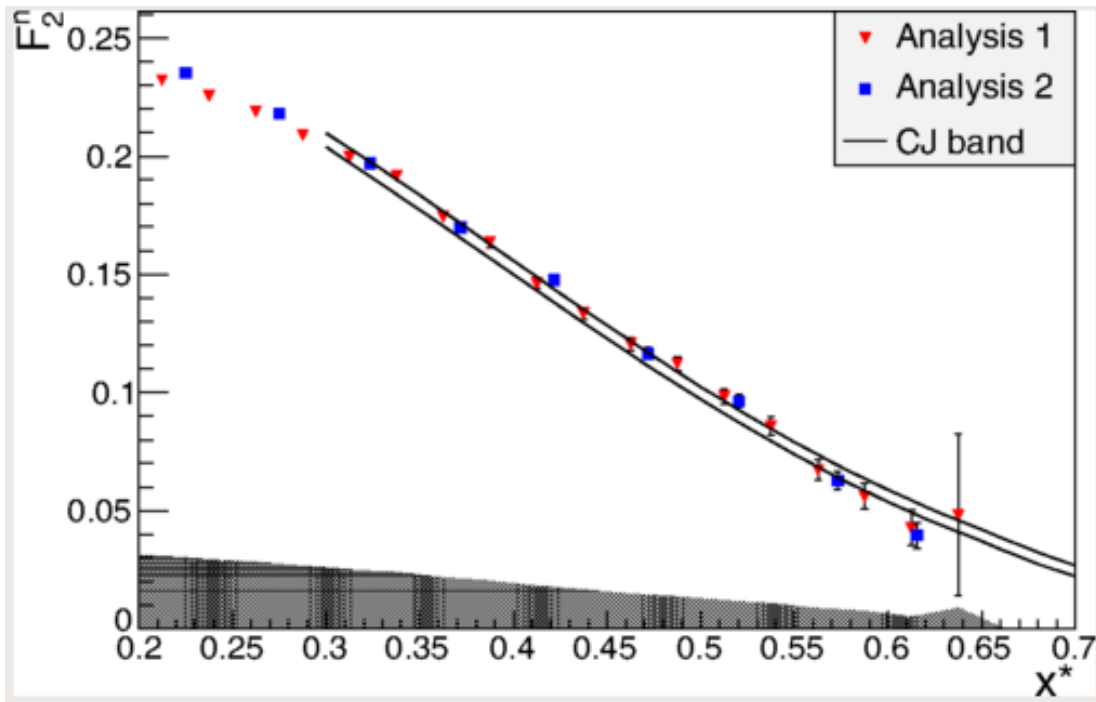
Figure 1.5: Results for the neutron structure function

$F_2^n(x)$(integrated over $Q^2 > 1GeV^2/c^2$ while requiring $W^* > 1.8GeV/c^2$) from the Monte-Carlo method (Analysis 1) and the ratio method (Analysis 2). The range of F_2^n from the CJ fit is shown by the two solid lines. Systematic uncertainties for the Monte-Carlo method are shown as the shaded band. The two analysis results are cross normalized to the average of the CJ fit at $x = 0.32$ [23].

The ratio F_2^n/F_2^p which was of high interest because of its relationship to the asymptotic d/u ration, was also extracted from the data using a suitable model for F_2^p. These results can be seen in Fig 1.6. In this figure, the results are shown for three lower cuts on the range for W^* over which the data was integrated over. The red triangles are for $W^* > 1.8 GeV$. In other words, showing the same data as Fig 1.5. The data is in agreement with the predictions from the CJ fit, but does not exted beyond the $x = 0.6$ range. The black squares $(W^* > 1.6 GeV)$ and the blue circles $(W^* > 1.4 GeV)$ pushes the limit to higher values of x [22].
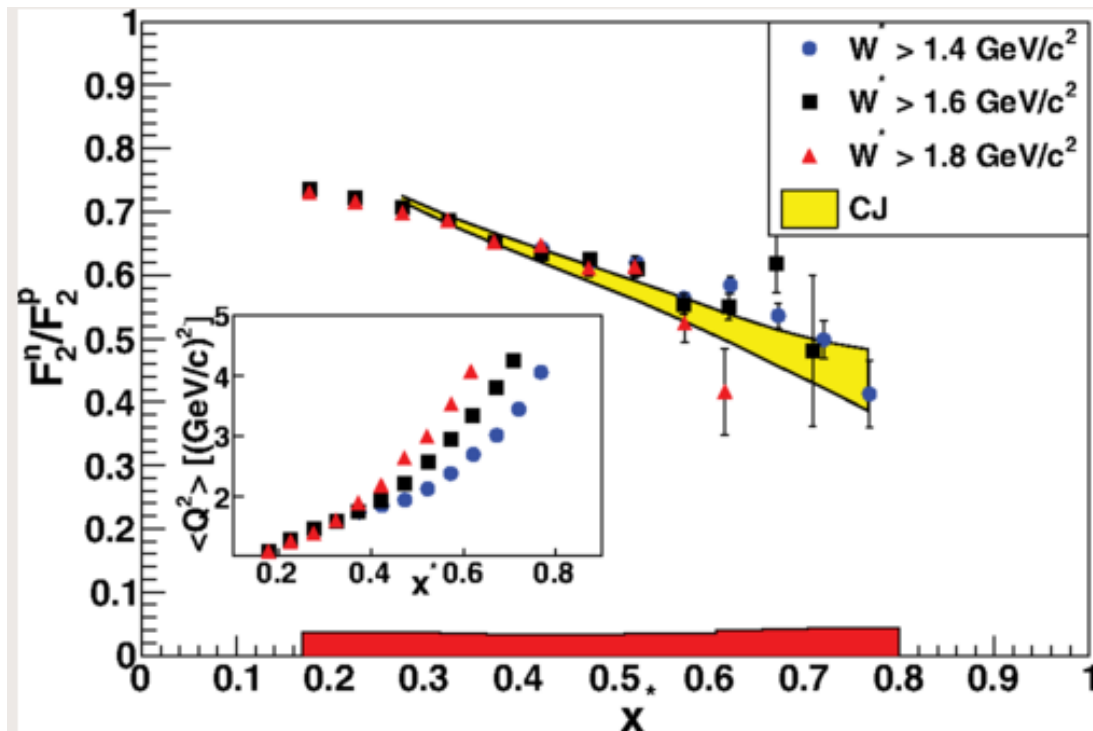
Figure 1.6: Results for the ratio of the neutron structure function $F_2^n/F_2^p(x)$ (integrated over $Q^2 > 1 GeV^2/c^2$ and three different minimum values for (W^*) from the ration method. The uncertainty range from the CJ fit is shown by the yellow shaded band. Systematic uncertainties are shown as the red shaded band at the bottom. The data was cross normalized to the average of the CJ fit at $x = 0.32$. The inset shows the average Q^2 for each data point, separately for the three lower W^* limits [23].

In an effort to improve of the results of this experiment, a massive upgrade was made to the accelerator facility and to Hall B to operate at 12 GeV. This beam energy upgrade will allow for the improvements on both the statistical precision and extend the range of X to 0.8. The need for this upgrade

will settle once and for all the question about the asymptotic behavior of the d/u ratio in the limit as x $\rightarrow$ 1 and complete the program of large x-measurements of the neutron structure function in the deep-inelastic-region [19]. This thesis will cover the upgrades made to Jlab and in Hall B in order to achieve these goals. In chapter 3, I will discuss the optimization of the RTPC and the environment that is present in the sensitive regions of this detector.

Chapter 2

EXPERIMENTAL SETUP
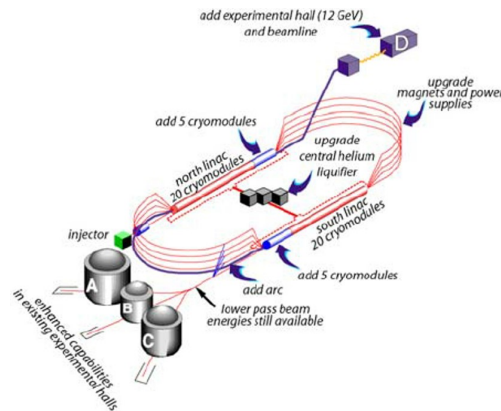
Figure 2.1: Layout of CEBAF

and the modifications for the 12 GeV upgrade.

2.1 Continuous Electron Beam Accelerator Facility (CEBAF)

The Continuous Electron Beam Accelerator Facility (CEBAF) is Jefferson Lab's main research facility. The beams fiducial region is located in the injector and then travels into the 7/8th mile underground racetrack shaped accelerator at nearly the speed of light in 24 millionths of a second. The accelerator is located in a tunnel about 25 feet below the ground on the Yorktown formation which is the remains of an ancient sea bed [1].

In 2012, the facility began a major upgrade project to double the maximum energy to 12 GeV, and add new experimental apparatus. The upgrade is focused into three systems: the Accelerator System, Physics System, and the Civil Construction System. The Physics System consists of upgrades to Hall A, Hall B, and Hall C. Primary goals of the 12 GeV CEBAF Upgrade include doubling the accelerating voltages of the linacs by adding ten new high-performance, superconducting radiofrequency (SRF) cryomodules (CMs), doubling the capacity of the existing cryogenics cooling plant, and adding eight superconducting magnets. The upgrade also includes the construction of a new experimental hall (Hall D) for dedicated research on exotic mesons produced by energetic photons incident on a target [4]. The main focus of

this thesis is the experiments in Hall B.

2.2 Schematic and parameters

The experiments conducted at Jefferson Lab utilize an electron beam that is originated by applying laser light onto a target composed of gallium-arsenide wafer that is approximately the size of a postage stamp. The laser light then energizes the electrons in the target, which cause them to flee their atoms. Electromagnets are then used to shape these free electrons into a coherent beam that has the thickness of approximately a human hair [1]. The electrons in this beam are grouped into a train of bunches of about one million each. More than 80 percent of these electrons are spinning in the same manner, or in other words, polarized. A schematic of the accelerator can be seen in Fig.2.2. Upon leaving the injector, he electrons are then
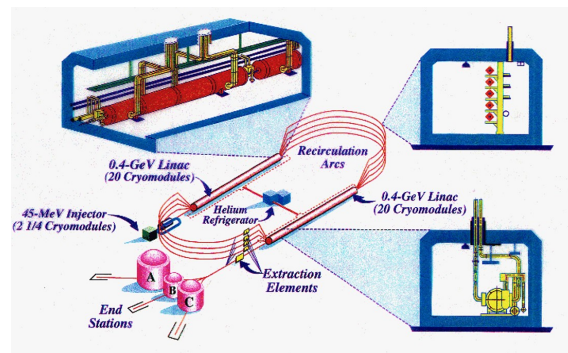
Figure 2.2: Schematic view of the accelerator

One of the cryomodules is shown in the upper left corner. In the upper right corner is a cross section of the recirculation arcs. In the lower right corner a vertical cross section of a cryomodule is shown.

accelerated to higher energies by passing through superconducting radio frequency (SRF) cavities. The electrons can then be circulated through the linear sections up to 5.5 times. These cavities are made of metallic niobium, which become superconducting at a temperature of 2 Kelvin [1]. These temperatures are extremely important since superconductors have no electrical resistance thus electrical current that is flowing through them does not lose any energy and produce no waste heat [2]. This temperature is maintained at Jefferson Labs Central Helium Refrigerator. The Central Helium Liquifier (CFL) cyrogenic system holds 17,000 gallons of liquid helium and runs 24/7 and is quite boastfully the worlds largest 2K refrigerator [1]. The cavities operate at 1.497 Hz, producing an electric field that accelerates the beam [1]. These cavities cannot be operated at room temperature because the heat

generated in this process would potentially melt the cavities [3]. Supercon-
ducting magnets powered up to 300 Amps (heaviest is about 20,00 pounds)
located in the recirculating arcs will drive and focus the beam, keeping it on
track in order to enter the next linear section as seen in Fig.2.2. The recircu-
lation arcs transport the beam between linacs. Once the beam reaches the
desired energy level, it is directed to the experimental halls. Each individ-
ual hall has its own strict beam energy requirements for the experimental
process. CEBAF can deliver the beam simultaneously to all four of the halls.
In halls A, B, and C the energy of the beam can reach 11.5 GeV and 12GeV
into hall D [1].

2.3 The 4 Experimental Halls

Jefferson Lab has 4 experimental halls where experiments are performed. In Halls A, B, and C, the electrons are typically smashed into the nuclei inside desired targets. These targets can be a solid, liquid, or a gas composed of any element, such as hydrogen helium. Most of the electrons will pass through the target unperturbed, but some will collide with the protons, neutrons, quarks or other particles inside. Behind the target sophisticated detector systems for capturing the outgoing electrons and other particles that may come out of the target via collisions. Hall A is the largest of these four experimental areas. The foundation for Hall A is 35 feet below the ground. Hall A is outfitted with two primary detector systems-both high resolution spectrometers, each weighing in at approximately 3 million pounds. The hall is primarily for experiments that study the structure of the nucleus and the protons and neutrons it contains. The experimental focus is on nucleon and few-body form factors, the strange quark structure of the proton, nucleon spin structure, and short-range nucleon-nucleon correlations. Hall B is the smallest of the halls at Jefferson Lab (JLab). This is the hall where the experiments for this thesis were conducted. Hall B is home to the CEBAF Large Acceptance Spectrometer (CLAS12) system. The detectors in Hall B were built and run by a collaboration of nearly 150 physicists from more than 30 different universities from all over the world. The goal for Hall B is to deduce the underlying structure of protons and neutrons in the target and to try to understand the forces that create these particles. The physics targets in Hall B include liquid hydrogen and deuterium. In experimental Hall C the Super High Momentum Spectrometer and the High Momentum Spectrometer are used to make precise measurements of the inner structure of protons and nuclei at high beam energy and current. Here multiple spectrometers are used to study parity-violating electron scattering to measure the weak charge of the proton and hypernuclear production with the electromagnetic interaction. Hall D is the newest of the 4 experimental halls. Experiments conducted here, the beam of electrons is steered into a thin sliver of diamond about one-fifth the thickness of a human hair. Some of the electrons are diverted by the diamonds crystal structure, emitting high-energy photons that then travel the length of a football field into Hall D. These photons then pass through a hole about the size of a grain of rice, ensuring that only perfectly aligned photons proceed toward the target. Then,

just as in the other 3 halls, detector systems measure the particles that result from collisions of the beam with particles in the target.

2.4   CEBAF Large Acceptance Spectrometer (CLAS12) in Hall B
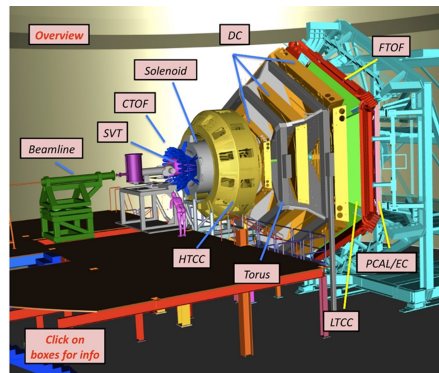
Figure 2.3: Diagram of CLAS12

In the attempt to satisfy the stern "physics quality" requirements of studying and probing hadron structure within a high accuracy regime, the infrastructure at Jefferson Lab has undergone major upgrades. One of these upgrades in particular included the CEBAF Large Acceptance Spectrometer for 12 GeV (CLAS12). The main new features of CLAS12 include operation with a luminosity of 1035 $cm^{-2}sec^{-1}$, which is an increase in order of magnitude over the past CLAS program [1]. This will allow more precise measurements for many exclusive reactions and higher resolutions. The CLAS12 detector also underwent enhanced particle identification at forward angles. The CLAS12 detector consists of two major parts, the Forward Detector (FD) and the Central Detector (CD). Each having unique and different functions. This is just a basic introduction and individual components of the CLAS12 experiment will be discussed in subsequent sections of this chapter.

2.5 The CLAS12 Forward Detector

A three-dimensional representation of the Forward Detector (FD) is shown in Fig.2.3. The CLAS12 forward detector is composed of the Drift Chambers(DC), a High Threshold Cherenkov Counter (HTCC), Forward Time of Flight (FTOF), a torus magnet, and Electromagnetic Calorimeters (ECAL/PCAL). Improved electron-pion separation at higher momentum is achieved with threshold gas Cherenkov counters for the detection of charged pions with momentum greater than 5 GeV/c [1]. The high threshold Cherenkov counter (HTCC) is positioned in front of the Torus magnet and is designed to present a minimal amount of material to charged particles traversing the HTCC [1]. This will minimalize multiple scattering and its impact on the momentum resolution. To achieve this, low mass composite materials were utilized as the basis for the mirror system, which presents less than 150 mg/cm of material [1]. The HTCC will be one of the detector system of the CLAS12 spectrometer and used to generate fast trigger signal in experiments with electron beam. The HTCC is one unit, and the core component of it is a multi-focal mirror consisting of 60 lightweight composite ellipsoidal mirrors. Each sector of the CLAS12 is covered with 2 identical half-sector mirrors that are focusing Cerenkov light on eight 5-inch phototubes (48 channels for entire detector) [1].

2.6 Superconducting Torus Magnet
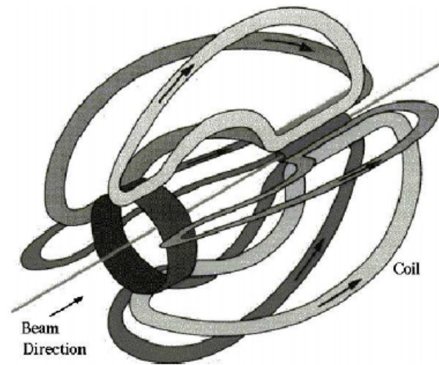
Figure 2.4: Diagram of torus coils

The CLAS12 forward detector contains a 6-coil torus magnet with a 3.6 T peak field. The torus magnet is one of two superconducting magnets utilized in Hall B that provide magnetic analysis of charged particles in the large-angle range and in the forward-angle range respectively. The magnets are separated by about 1.5 m, and their respective fields are partially overlapping. Due to the symmetry properties, the toroid field will drop with distance and has virtually no impact on the solenoid magnet [6]. In particular, since the field is zero on the beam axis, it will not affect the homogeneity of the solenoid magnet in the critical target region. The solenoid field drops more slowly with distance and exerts a force that can be measured on the coils of the torus magnet that must be taken into account in the design of that magnet [1]. At the closest distance between the solenoid and torus magnets, the coil deflection is about 1.3 mm, which due to the cylindrically symmetric solenoid field, affects all torus coils in the same way. The torus field is strongest at small polar angles and weakest at larger angles [1].

Once the beam interacts with the target, the momentum of the charged particles and electrons will be calculated by measuring the curvature of their trajectories in a magnetic field. The choice of this configuration leads to an approximate toroidal field distribution about the beam axis. It has been driven by the necessity of satisfying the following requirements: there needs to be uniform coverage of a large momentum and angle range with symmetry around the beam axis, an open structure that allows for long path lengths for charged and neutral particles resulting in good particle identification through precise time of flight measurements, and low background

from electromagnetic processes to reach high luminosity. These coils do not contain any iron so the resultant field can be determined solely by the current within the coils. The entire magnet has a diameter of 5 meters and is 5 meters in length [1]. The six sectors combined produce an azimuthal magnetic field which is most uniform at the midlines between the coils. The vector fields become largest and less regular near the coils but have no tracking volume at the coils or in the projected volume behind them. Having an accurate field map within the tracking volume is essential to produce accurate momentum measurements. The highest field value is measured to be 2.5 $T \cdot m$ with a current of 3860 A at forward angles. The $B \cdot dl$ will drop off to 0.6 $T \cdot m$ at 90 degrees. The coil operating temperature of 4.5 K is maintained by a forced flow of supercritical liquid helium [3][7].
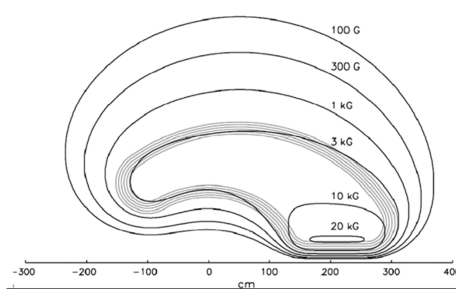
Figure 2.5: Lines of constant magnetic field in the center of the area between two torus coils.

The outline of the coils is seen as a multiple-lined "kidney bean".[3]

The particles can be bent towards or away from the beam axis to sweep low-angle particles into or out of the detector acceptance. In the area at the very center between the two coils, there is no deflection in the ϕ direction although there will be some small deflection in the ϕ direction will occur for tracks not on the center line. In the BoNuS experiment the current was set at 1500 A when the electron beam was at an energy between 1 and 2 GeV and 2250 A for a beam energy of 4 and 5 GeV. This produced an electron momentum of about 1 percent after calibration. The various tracking and energy devices naturally fall into a six-segment geometry configuration around the six coils. Each section is identical except they were rotated $60°$ in the ϕ-direction. This configuration yields six blind spots in ϕ where the coils are physically mounted, each covering $\Delta \approx 20°$ each.[3]. The torus magnet

was delivered in 2010 and took approximately 6 months to assemble [6].

Due to the stored energy of approximately 14 MJ, the magnet system will be protected by a quench detection and protection system. In the event of a quench, the energy stored will be dissipated in a resistor dump that is specially designed to keep the voltage below 500 V.[6] For more detailed information on the magnet system utilized in Hall B, see [6].

2.7 Drift Chambers

A "wire chamber" is a particular kind of particle detector. Essentially it is a large box constructed with small-diameter fine wire crossing from one side to the other and are filled with a special gas. The wires are run at high voltage with some positive voltage and some at a negative voltage. In order to conceptualize how this works, the analogy to observing a jet flying overhead can be used. A high-flying jet may be invisible but the condensed vapor trail or "contrail" is visible to the eye, which gives the path of the jet Fig.2.6. A charged particle is too small to see directly, but when that particle
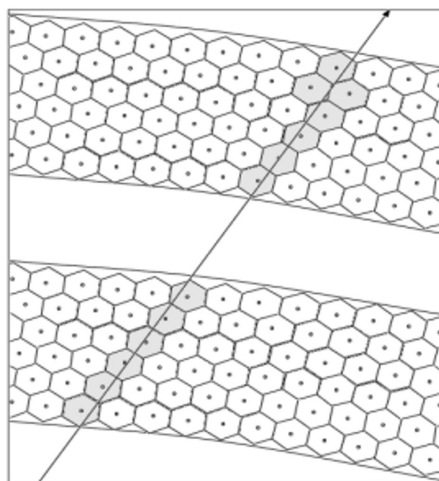
Figure 2.6: Drift Chamber section showing two super-layers.
The arrow shows a charged particle passing through the drift chamber.

passes close to gas atoms, electrons can be knocked free and leave behind a trail of electrons. These electrons have negative charge so they are attracted to the wires which are at a high positive voltage. When the electrons arrive at the wire, they create an electronic signal which is amplified and then subsequently recorded. By observing which wires displayed electronic signals, the path or track of the particle can be determined just as the path of the jet flying overhead could be determined. The tracking is more accurate if the timing of the signals is deduced as well. By doing these deductions, the distance from the wire to the particle can be extrapolated.

The first detector elements encountered by the final state particles are the drift chambers. Each of the six sectors has three drift chambers at increasingly larger radial distances from the beam line. There is a total of 18 separate wire drift chambers; each with 2 superlayer of 6 layers by 112 wires
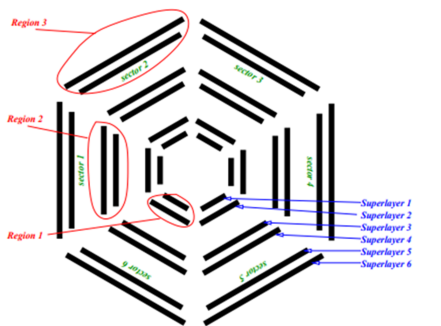
Figure 2.7: Layout of the drift chamber.

This view represents a vertical slice through the drift chambers at the target position looking downstream. The schematic shows how the regions and superlayers are placed and named [2].

giving a total of 24,192 sense wires [1] .The wire direction is perpendicular to the bend plane. The chambers can track particles with a polar angular range from 8-142 degrees and momentum >200 MeV/c [3]. The design resolution goals were 0.5 percent for momentum and mrad for the scattering angle. Region 1 (R1) is in the area of the smallest field and closest to the target. Region 2 (R2) is in the middle of the coils where the highest field and azimuthal displacement occurs. Region 3 (R3) lies outside of the torus magnet [1][3]. The tracks are measured at three points to an accuracy of 100 micrometers in the bend plane (containing the beamline) and 1mm perpendicular to the bend plane. The amount of material is < 0.01 radiation length in the tracking region [3].

Each chamber is divided into two superlayer in order to obtain track redundancy and increase pattern recognition. One superlayer has wires axial to the magnetic field and the other has its wires tilted at 6 degrees. There are six layers of drift cells in each superlayer (except R1 where there are 4). The cells are hexagonal in shape and there are 35,000 cells in total [1]. A signal wire lies at the midpoint of each hexagon with field wires at the vertices. There are guard wires at the edges of the chambers held at a high voltage intended to mimic an infinite grid of drift cells. The gas gain is a few times 104 and the electric field at the surface of the sense wires is approximately 280 kV/cm. To minimize cathode deposits, the field at the surface of the field wires is < 20 kV/cm. The drift chambers are filled with a typical ionization detector gas mixture of Argon-CO_2 in a 9:1 ratio that provides a

saturated drift velocity of 4 cm/microseconds [3].

The drift time for each channel must be known in order to optimize position resolution in the drift chambers. Environmental conditions in the experimental hall, such as atmospheric pressure, humidity, etc., change the drift chamber gas properties. The drift can also depend on the particle's entrance angle and velocity and the local magnetic field. Once a reference time is determined in the scintillation counter, the TDC time on the sense wires can be analyzed to the reference value and then can be parameterized according to Eq.2.1 as seen below,

$$x(t) = v_0 t + \eta \left(\frac{t}{t_{max}} \right)^q + \kappa \left(\frac{t}{t_{max}} \right)^p. \tag{2.1}$$

Where t_{max} is the maximum drift time and v_o is the value for the saturated drift velocity near time t is equal to zero. The parameters , and p are determined by minimizing

$$x^2 = \frac{|x(t) - x_{path}|^2}{\sigma_{path}^2}. \tag{2.2}$$

Where x_{path}, σ_{path} are the distances of closes approach (DOCA) from the sense wire along the path and the error on this quantity, respectively [3].

The quality of the calibration is measured through the spatial residual where the lowest possible value is preferred. The calculated value x(t) can be found in Eq.2.1. More details about the drift chambers along with a sample of the resolution of the residuals for the experiment can be found in [8]

2.8 CLAS12 ECAL-PCAL (EC)
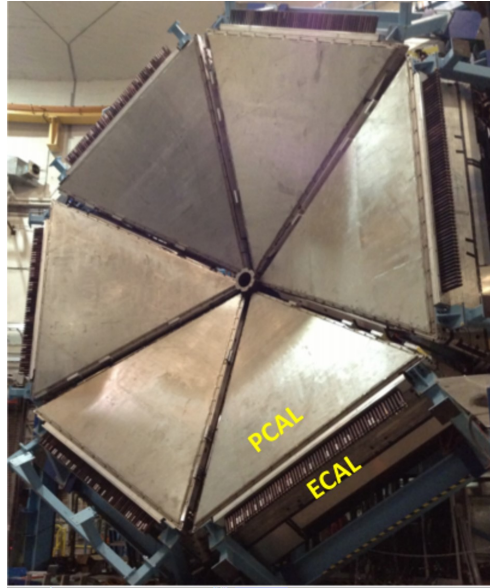
Figure 2.8: ECAL/PCAL layout.

The main function of the CLAS12 electromagnetic calorimeter (EC) in the BoNuS experiment is to provide identification of electrons, photons,$\pi^o \rightarrow \gamma\gamma$ decays, and neutrons [1]. The pre-shower calorimeter (PCAL) and electromagnetic calorimeter (EC) are sampling calorimeters both consisting of six modules. Each of these modules are triangular shaped oriented in a flower pattern about the beam line with 54 (15/15/24, PCAL/ECAL-inner/ECAL-outer) layers of 1 cm thick scintillators segmented into 4.5/10cm (PCAL/ECAL) wide strips and sandwiched between 2.2 mm thick lead sheets as seen in Fig.2.8 [1].

The lead sheets are used to produce electro-magnetic showers and the scintillator layers are used to measure the timing, location and the energy of the charged particles in the subsequent showers. The calorimeter uses a "projective" geometry, in which the area of each subsequent layer will increase in order to minimize leakage at the edges of the active volume and also to minimize dispersion in arrival times of signals that originate in different scintillator layers.[1] The strip orientation is rotated 120 degrees from layer to layer in order to provide stereo information on the location of the shower labeled U,V, and W in Fig.2.9 [3].

A typical reconstructed event in the EC can be seen in Fig.2.8. The target
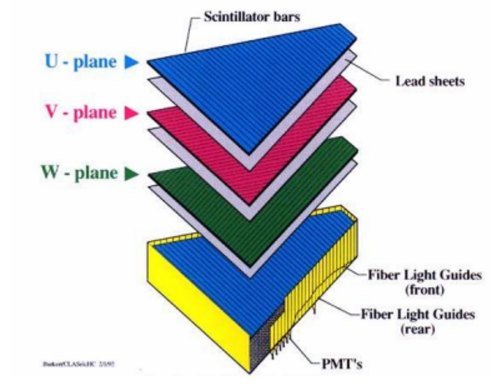
Figure 2.9: Exploded view of electromagnetic calorimeter in one six sectors.

EC resolution is $\frac{\sigma}{E} \leq \frac{0.1}{\sqrt{E(GeV)}}$ with a position resolution of $\delta r \approx 2$ cm at 1 GeV. Separation of pions from electrons is accurate almost every time, with proper cuts on energy deposit on the inner and outer portions of the detector [3]. Although the entire background of pions could potentially be removed from the electron sample, too many good electrons would be lost [3].

Following the LTCC are three arrays of plastic scintillators for precise Time-of-Flight measurements (FTOF) for charged particle identification. Scintillators generate photons in response to incident radiation where a sensitive photomultiplier tube will convert the light into an electrical signal which can be processed via electrical equipment. The new first layer consists of 60x60 mm thick bars of plastic scintillators. They provide highly accurate timing data of $\delta T = 30 - 80$ psec depending on the length of the scintillator bar, the best resolution of any existing detector system based on plastic scintillators. The other two layers are being refurbished from prior CLAS experiments for equal pion, kaon, and proton yield that will enable a pion/kaon separation of 4σ for momenta up to 3 GeV/c, and a kaon/pion separation up to 4.5 GeV/c from time-of-flight measurements alone [1]. Aspects of the experimental program that require the identification of pions and kaons with momenta up to 8 GeV/c is achieved by replacing individual LTCC detectors with Ring Imaging Cherenkov detectors (RICH). For CLAS12, one or more of the RICH detectors will be utilized [1] .

Large parts of the physics program will require the identification of single

high-energy photons and the separation from $\pi^o \to \gamma\gamma$ up to 9 GeV/c.[1] The granularity of the existing electromagnet calorimeter (EC) will be improved by adding a pre-shower calorimeter (PCAL) of ≈ 5 radiation length in front of the EC. This layout will provide a factor of 2.5 better spatial resolution and the separation of two photons for momentum up to 10 GeV/c [1]. In the very forward direction for angles below 5 degrees, a Forward Tagger (FT) system will detect small angle scattered electrons using a lead-tungstate inner calorimeter (IC) which consists of 400 crystals and a set of scintillator strips and tracking chambers. The crystals will also provide high energy γ and π^o identification for momenta up to 10 GeV/c [1][2].

2.9 Scintillation Counters

An array of scintillators and photomultiplier tubes make up the CLAS12 time-of flight (TOF) system.[9] A section of this array is seen in Fig.2.10. This array is responsible for the identification of particles using tracking information from the drift chambers along with high-resolution time of flight measurements.
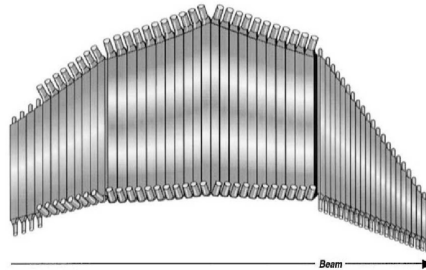
Figure 2.10: TOF scintillation counters in one of the sectors.

The vertical rectangles are the scintillation bars and the cylinders at the ends are the photomultiplier tubes.

The scintillation bar design is essentially a uniform wedge-shaped piece of BC-408 scintillator material that subtends a 7.5 degrees azimuthal range as seen from the target.[1] Only at the very ends of the bars have upwards curvature to join the light guides as seen in Fig.2.10.

The system is capable of separation of pions and kaons. Each scintillation counter (SC) covers 1.5″ in polar scattering angles. The forward counter are 15 cm wide and the large angle counters are 22 cm wide. The counter length will vary from 35 cm to 445 cm. The TOF counters operate in a high rate environment produced by luminosities above 10^{34} $cm^{-2}sec^{-1}$.[3] The average rate per scintillator is approximately 100 kHz.[3] Photomultiplier tubes, light guides, voltage dividers and cables are located further from the beamline that the torus coils and the Region 3 drift chambers and are in the shadow of the coils to shield them from scattered particles [3]. The active area is made up of 5.08 cm thick Bicron BC-408 scintillators [1]. The thickness was chosen to give a large enough signal to separate minimum-ionizing particles from the background particles. The fiducial volume covers 206 m^2 and the PMTs are magnetically shielded [3].

2.10 Superconducting Solenoid Magnet

The Central Detector (CD) is based on a compact solenoid magnet [6]. A three-dimensional view of the Central Detector (CD) subsystems is shown in the Fig.2.3. Solenoid magnets provide the most ideal field distribution for analyzing the particle trajectories in the central region of the detector. This occurs where the bending power of the solenoids magnetic field is at its maximum. The solenoid magnet provides a strong magnetic field needed for a dynamically polarized solid-state target [6]. The solenoid field is also utilized for particle tracking and momentum analysis by measuring the trajectories of charged particles in the field with high-resolution tracking detectors. For the CLAS12 experiment a 5 T strong solenoid field has been driven by the necessity for the following parameters dictated by the program: a large opening for charged and neutral particles in the forward hemisphere since high forward-going particles will not experience high enough transverse field components from the solenoid and must be momentum analyzed in the torus field located downstream of the solenoid magnet [1].

The solenoid magnet provides momentum analysis for charged tracks at polar angles from 35 degrees to 135 degrees. It also protects the tracking detector from intense background electrons and acts as a polarizing field for polarized solid-state targets [3]. All of these functions require a high magnetic field along the beam axis. The size of the solenoid is restricted to 200 cm in diameter, which allows a maximum warm bore for the placement of detector of only 80 cm in diameter [1]. In order to obtain sufficient momentum resolution in the limited space that is available, this requires high field and precise position resolution of the tracking detectors. The central field in the target region must also be very uniform at $\frac{\delta B}{B} < 10^{-4}$ to allow for the operation of a dynamically polarized target [1][2][6]. In order to achieve a sustained high polarization for polarized ammonia targets (NH3 and ND3), this requires a strong magnetic field. Magnetic fields at 5 Tesla are currently used for such targets with polarization of up to 90 percent for the free hydrogen in NH3. The solenoid field guides the mass produced Moller- electrons away from the sensitive detectors to locations; where they can be passively absorbed in tungsten absorbers [1][6]. The solenoid magnet will be made of a total of 18 modules, where individual modules composed of double pancakes [6]. The central field homogeneity is produced through adjustments of the outer and inner diameter of each individual module. To help

in spreading the quench through the coils, a heater will be utilized in order to prevent a local hot spot from proliferating. Active quench detection will constantly monitor critical voltages from within the magnet [6]. In the event of a quench the power supply will be deactivated and discharge the magnet into a dump circuit [6].

Central Tracking system

Charged particle tracking in the CD is provided by the Silicon Vertex Tracker (SVT) as seen in Fig.2.11, which uses silicon strip technology to measure the momentum and determine the vertex of charged particles emerging from the target [1]. The SVT system includes 4 regions with 10,14,18, and 24 sec-
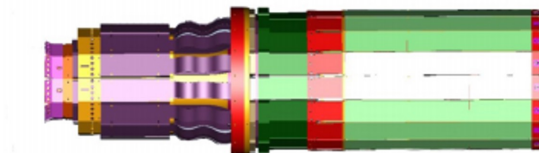
Figure 2.11: Diagram of the CLAs12 silicon vertex tracker (SVT).

tors of double-sided modules (silicon sensors on both sides of the backing structure) instrumented with digital readouts [1]. This system is designed to operate at a luminosity of $10^{35}cm^{-2}s^{-1}$ and has a momentum resolution of ≈5 percent for 1 GeV particles emerging from the target at $\theta = 90°$.[1] The SVT is made from 8 stereo layers of silicon sensors and provides tracking for polar angles ranging from $35°$ to $135°$. At larger radii, 3 double layers of micromesh (MM) gas detectors provide additional tracking that improves momentum and polar angle resolution dramatically [3].

Central Time of Flight System

Particle identification is acquired in the central time-of-flight scintillator array (CTOF) as seen in Fig.2.12 which consists of 48 92-cm long scintillation bars of fast plastic scintillator equipped with 96 photomultipliers that provide 2-sided light readout and a timing resolution of $\delta T = 60$ psec [1]. The
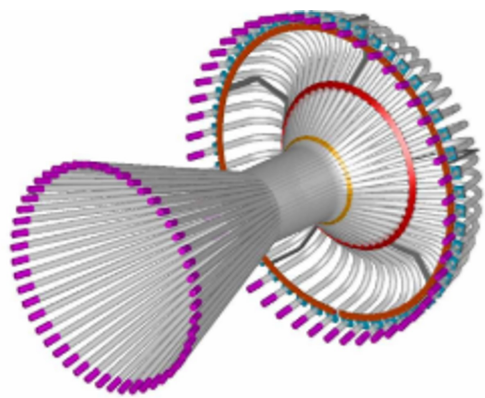
Figure 2.12: Diagram of the Central Time Of Flight stytem (CTOF).

CTOF detector will be mounted to the CLAS12 solenoid magnet. The global z-axis, the beamline, lies along the symmetry axis of the CTOF barrel pointing downstream (left to right in Fig.2.12). The global-axis points upward in the same figure. Specially shaped light guides bring the scintillator light to an area of reduced magnetic field where a combination of passive and active magnetic shielding is used to allow operation of photomultiplier tubes. The short flight path from the target to the CTOF array allows for particle identification in a momentum range of up to 1.2 GeV/c and 0.65 GeV/c for $\frac{\pi}{p}$ and $\frac{\pi}{k}$ separation respectively [2].

In some experiments, the detection of fast neutrons in the central angle range is needed. To accomplish this, the central neutron detector (CND), a barrel consisting of 3 layers of 48 scintillator bars, will be employed which provides neutron detection with efficiencies of 10-15 percent [3][1]. Two neighboring bars are connected through a half circular light guide on the downstream end with photomultipliers attached at the other ends.

Deuterium Target

If the desired goal of the BoNuS12 experiment is to be met, it is imperative to be able to detect low-energy spectator protons. This is the motivation to employ a Radial Time Projection Chamber (RTPC) (which will be discussed in the detain in another section) with a gaseous deuterium target. Given the nature of spectator protons which have momenta less than 150 MeV/c, a liquid or solid target would not suffice because the spectator proton would not have enough energy in order to escape [2]. The target wall needed to be constructed of a material that had a small radiation length and was structurally strong enough so that the thickness could be reduced as much as possible. These are the reasons as to why the gas deuterium target under 7 atm and room temperature was selected. Kapton that had a thickness of 50 μm was used to construct the target straw with an inner diameter of 6mm with a 15 μm aluminum cap at both ends of the target window. The total length of the target straw is 280 mm with 210 mm covered by the RTPC [1][2]. On the upstream end there is an aluminum collar, which limits forward moving particles from causing signals in the RTPC. Given this, the viable target length is about 160 mm [1]. The downstream part of the target straw was surrounded by a helium gas tube in an effort to minimize the background. Deuterium was the preferred production target for the bulk of the data but gaseous hydrogen and helium targets were employed for calibrations [1].

2.11 Radial Time Projection Chamber (RTPC)

One of the new pieces of equipment that was built for the BoNuS 12 experiment is Radial Time Projection Chamber (RTPC). The idea of utilizing the RTPC was brought up by detector expert Howard Fenker [3]. The addition of the RTPC which uses Gas Electron Multipliers (GEM), sets the BoNuS 12 experiment aside the previous CLAS experiments. This chapter will cover the motivation, construction, and design of the RTPC.

Design Motivation, Constraints, and Geometry
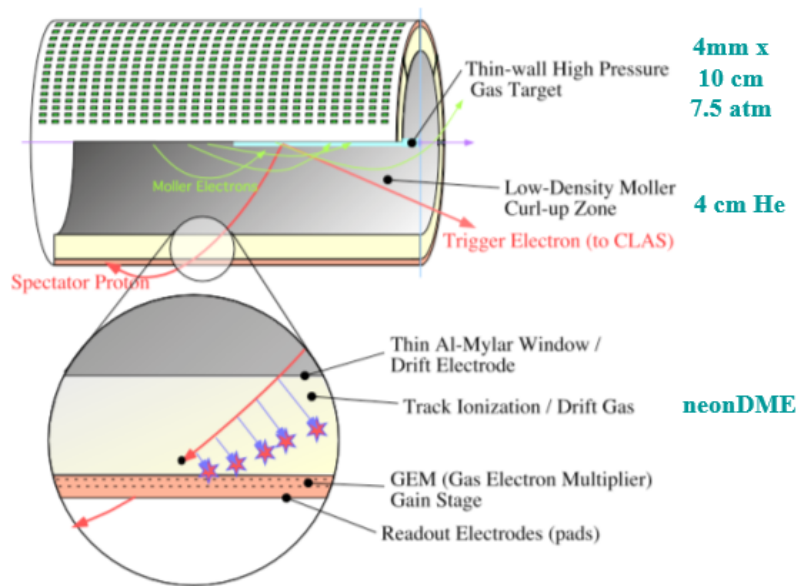
Figure 2.13: Diagram of the planned RTPC.

The Barely-Offshell Nucleon Structure (BoNuS) detector is a RTPC that will be installed within the CEBAF CLAS 12 at JLab Experimental Hall B. The main goal of the BoNuS experiment is to detect slow, backward-moving spectator protons from a deep inelastic collision of electrons on neutrons in the gaseous deuteron target with a Kapton wall of only 50 micrometer thickness. The focus of this experiment is to gather data and measure the $F2$ structure function of the neutron, of which there is currently little data. The two main features of this detector are: radial time projection because of its fast response and low energy threshold so as to minimize the energy loss of the particle before it reaches the drift region [2]. A detailed diagram of the RTPC is shown in Fig 2.14.

Time Projection Chambers (TPC) were first invented in the latter parts of the 1970's at the Lawrence Berkeley Laboratory [3]. Anode wires with end-cap readout strips for the signal amplification and collection were utilized. TPC's are commonly used in collider experiments in order to obtain measurements of 3D particle tracks in a high-rate environment. A TPC, like a bubble chamber, can simultaneously make measurements of the track and specific energy loss, dE/dx, of many particles [3]. Due to the TPC's fast and all digital readouts, it has been seemingly referred to as an electronic bubble chamber. TPCs are utilized to measure the path of the track at many points,
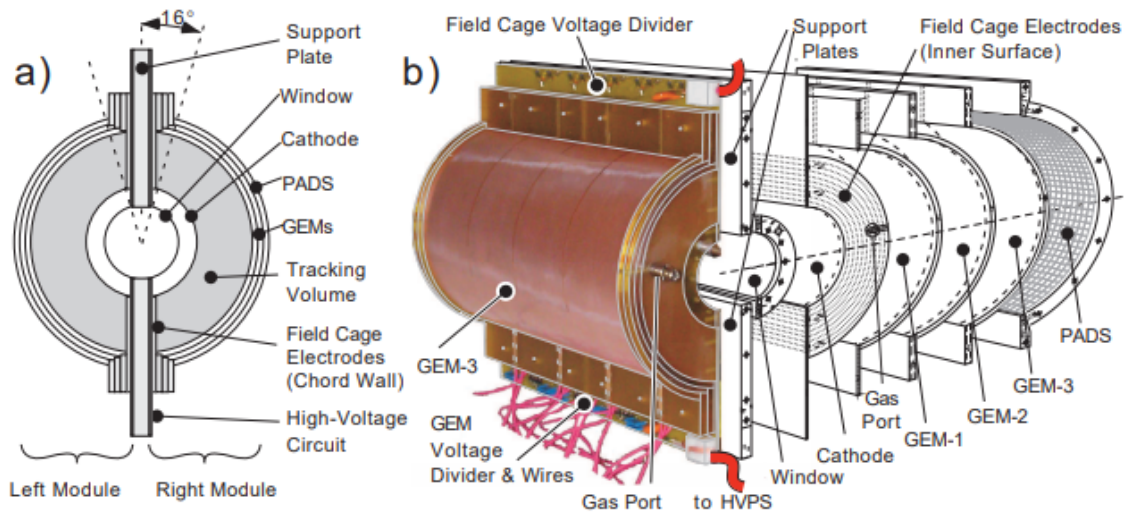
Figure 2.14: On the left is a cross sectional view of the RTPC as seen from downstream. On the right is the RTPC's left section next to an exploded view of the right section.

which yields position and momentum resolution. The timing resolution enables a highly accurate measurement of the energy that is deposited in each volume element (voxel) to achieve particle identification [3]. These TPCs are constructed in a cylindrical design so that the magnetic field, electrical field, and the central axis are all parallel. This configuration will cause ionized electrons to move at a constant speed and in a straight-line path.

For the use of the BoNuS 12 experiment at JLab, this convention design of TPCs is not ideal for several reasons. The first reason is that the forward scattered electrons would encounter a large amount of material on the downstream endcap of the TPC which would cause more energy loss before the particle encountered the tracking system than what is preferred [3]. The second reason is that the magnetic field that is produced by the solenoid magnet has a non-negligible radial component which becomes larger at each end of the magnet [3]. This would cause a large quantity of electrons to not be collected as they would subsequently be driven into the walls of an axial-drift time projection chamber in this given field. For the purposes at JLab, a radial-drift time projection chamber will be utilized where the path of the electrons traverse in a constant z-direction but vary in the r and ϕ -directions respectively. Another downside is that the endcaps of traditional TPCs have Multi-Wire Proportional Chambers (MWPC)

that require fairly massive components in order to maintain wire tension would not fit given the diameter of the solenoid at JLab. Also, utilization of these MWPCs cause high numbers of positive ions from avalanches drifting back in the direction of the cathode, which, overtime will pile up causing a distortion in the drift field [3].

The BoNuS 12 detector is composed of a $3mm$ deuteron target surrounded by a 50 micrometer Kapton wall, a ground foil at $20mm$ and cathode at $30mm$ to generate the electric field [Nate]. The ionization occurs in the sensitive regions at $30mm$ to $70mm$. The RTPC at JLab, is divided into halves by their supporting bed plates, which cover 180° in the azimuthal angle and are $20cm$ in length [2]. From the downstream end, the RTPC is composed of six coaxial cylinders, each having its own function. The first cylinder is constructed out of aluminized mylar $(C_{10}H_8)$ foil (6.4 micrometer thick mylar with 0.035 micrometer thick aluminum on both sides) and is the inner window located at $r = 2cm$ [2]. Located at $r = 3cm$ is the second cylinder which is also fabricated out of the same mylar foil as the first. This cylinder acts as the cathode of the drift region. The last three cylinders are the Gas Electron Multiplier sheets, which in order are attached at $r = 6.0, 6.3,$ and $6.6cm$. These sheets are constructed out of copper-surfaced Kapton $(C_{22}H_{10}N_2O_5)$ foil (50 micrometer thick Kapton with 5 micrometer thick copper on both sides) [3].

For the BoNuS 12 experiment, the target gas cell length will be doubled which leads to doubling the luminosity, a reduction in data taking time all while keeping the event to background ration constant [19]. Utilization of a single GEM foil for a specific GEM plane along with a cylindrical arrangement, the 64 degree inactive azimuthal region can be reduced to an inactive region of 10 degrees [19]. This causes the effective tagged region d(e,e'p)X will increase significantly by a factor of two. A highly useful byproduct of an increased range of angular backward scattering angles of the protons is that the position (momentum) resolution will not be lost and the number of readout channels will consequently be doubled.

In order to improve the momentum resolution of the spectator protons, the effect of increasing the radial drift region from $3cm$ to $6cm$ was studied. The addition of track length of the RTPC yielded higher momentum spectator protons to be more pronounced and gave us the ability to extend the mo-

mentum range to higher values.

Custom Gas Electron Multipliers
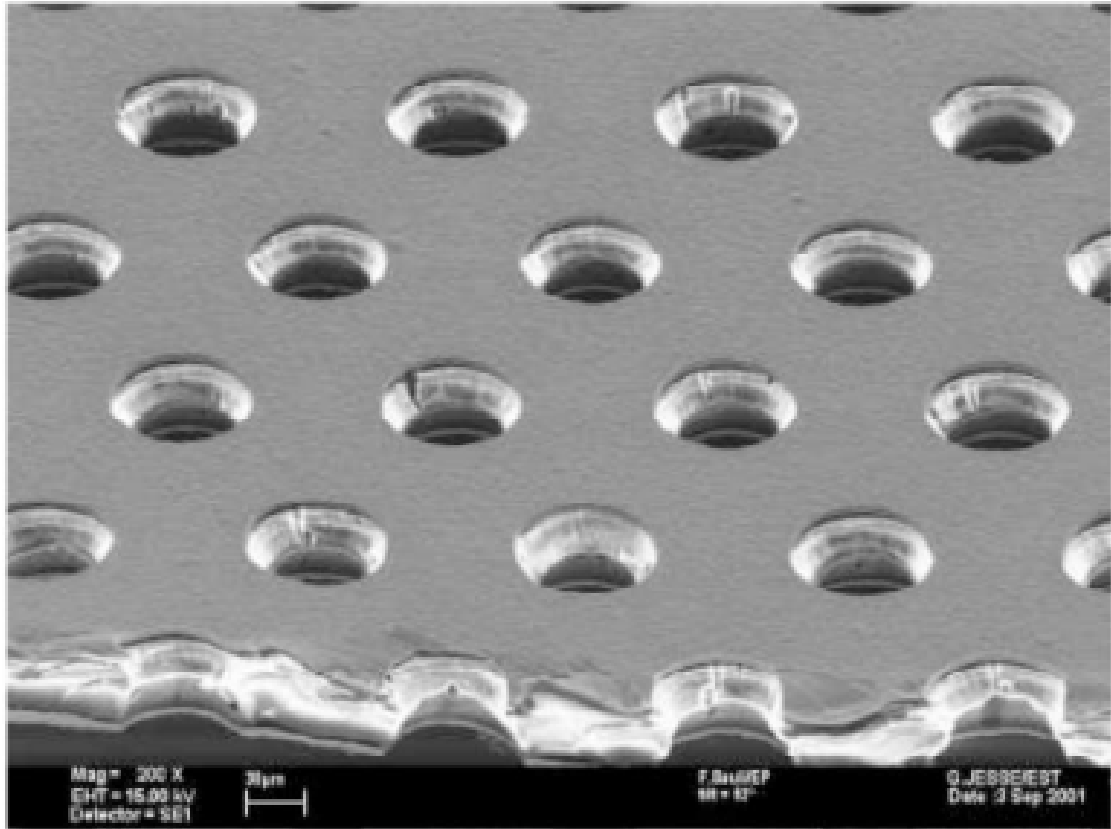
Figure 2.15: A generic GEM foil as seen through an electron microscope.
This image is approximately 400 micrometers across.[3]

The Gas Electron Multiplier (GEM) is a composite grid which consists of two metal layers that are separated by a thin insulator and are acid etched with a regular matrix of open channels. When the electrodes are kept at a desired potential difference and placed in a gas detector in the path of drifting electrons, allows to pre-amplify the charge that is drifting through the target regions. When coupled with devices such as multiwire chambers, GEMs will allow to obtain higher gains or to perform in less than desired experimental conditions. [19] The Gas Electron Multipliers (GEM) used at JLab as seen in Fig 2.15 are 50 micrometers thick polyimide foils coated on both sides with a 5 micrometer thick copper layer and are punctured with 70 micrometer holes. These holes are about 140 micrometers apart and are arranged in a hexagonal pattern. When a voltage from 200V to 300V is applied across the two copper layers, a large electric field in produced inside the holes. Electrons that drift in the direction of the GEM foil cause an

avalanche of secondary electrons when they are captured and accelerated through the holes. This causes a gain of in the order of 100. The ionized electrons are then sent to the next GEM foil and then to the next.

In particular, Gas Electron Multipliers yield high value to the BoNuS 12 experimental needs. The foil is thin enough so that it can be curved in a cylindrical shape. One challenge that the engineers faced was to keep it from wrinkling during construction. These devices have no preference in orientation or readout shape due to the fact that they have no uniform surface over which amplification can occur [2]. This thin GEM foil provides a low amount of energy loss when it comes to particles that are scattered. Custom GEMs were produced for JLab by the Tech-Etch corporation that have an active area covering 20 cm x 17 cm. The double-conical cross section is produced by under-etching the polymer to produce the hour glass shape [3]. After passing through three GEM foils, the pulse is then detected on the readout plane. In regards to the BoNuS 12 experiment, a new layout of a continuous foil for each GEM plane cylinder will be designed which will ultimately increase the azimuthal acceptance of the detector.
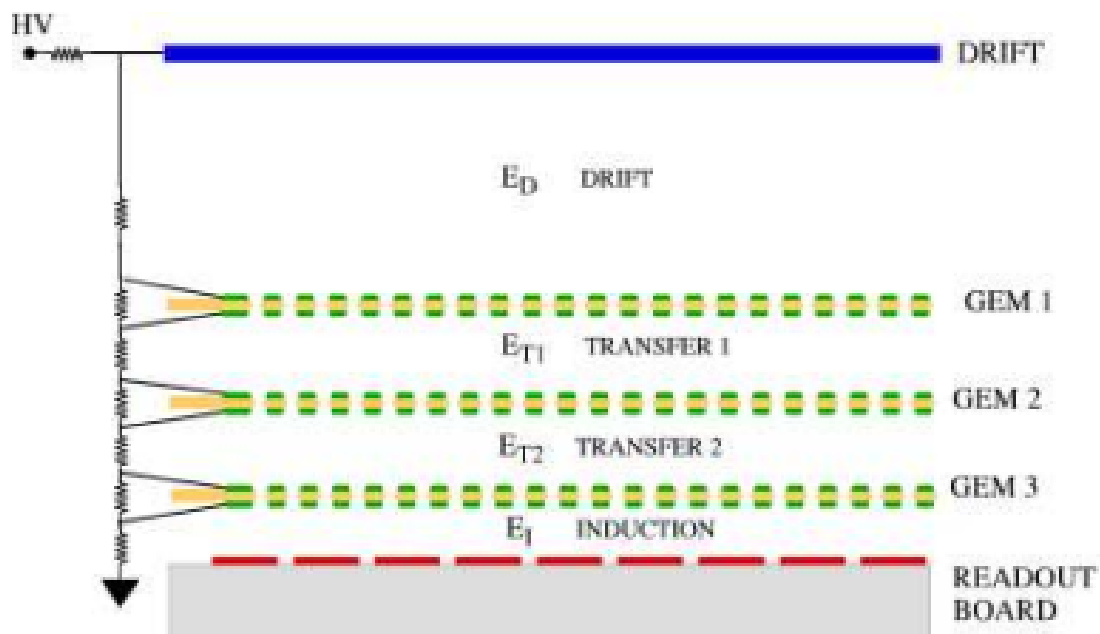
Figure 2.16: A schematic of each layer in a standard tripple GEM detector [3]

Readout Electronics

The outermost cylindrical layer of the detector is the readout board made of a flexible polyimide substrate [19]. The inner surface carries gold-plated conductive pads with a pattern of 4.45 mm x 5mm as seen in Fig.1.20. The brick layout makes sure that all tracks with θ between 87.5^o and 92.5^o are not assigned $\theta = 90^o$. The pads are connected by closed bias to the outer surface on which groups of 16 pads are traced to a common connector, carrying 16-channel preamplifier cards [19]. The acquired signals are inverted on the cards and sent through 6m long cables to a low-impedance receiver circuit which send positive signals into the readout electronics that were initially developed at CERN for the time projection chamber for the ALICE experiment at the LHC for heavy ion collisions. [20]. Each readout card has 128 channels of pre-amplification, digitization via a 10-bit ADC, signal correction units, and a pipeline buffer for eight event.[19].
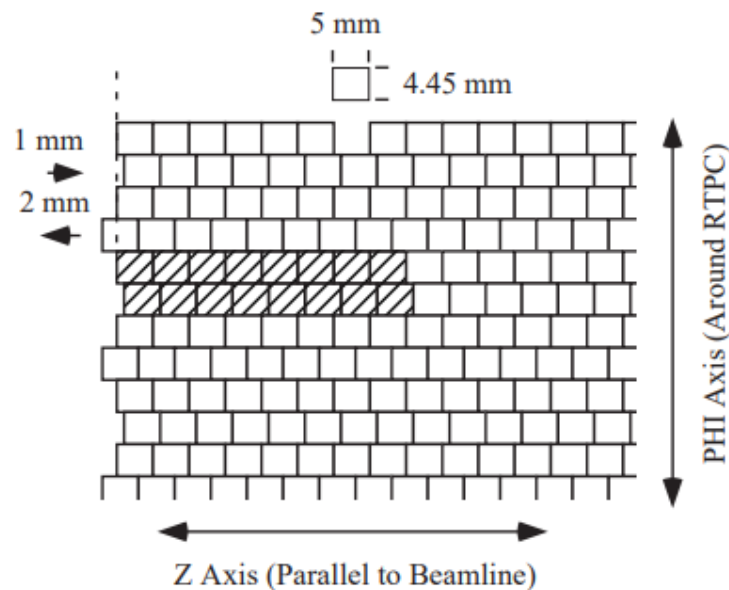
Figure 2.17: Pad layout in the production of the RTPC.

There are 40 rows and 40 columns of pads per detector half. The shaded area shows a group of pads read by the same preamp.[3]

The signals of all the pads are integrated over 114 nsec time intervals for a period of 1.7 microsecond before and 9.7 microsec after the arrival of an electron trigger from CLAS [19]. Each pad is connected electrically connected to the opposite side of the the board with traces leading to a commercial

connector pattern. Each of these connectors carries sixteen pad signals and supports a pre-amplifier card. A schematic for one preamp is seen in Fig. 2.18. In total there are 200 of these cards for the RTPC, with each side consisting of 100 cards [3].
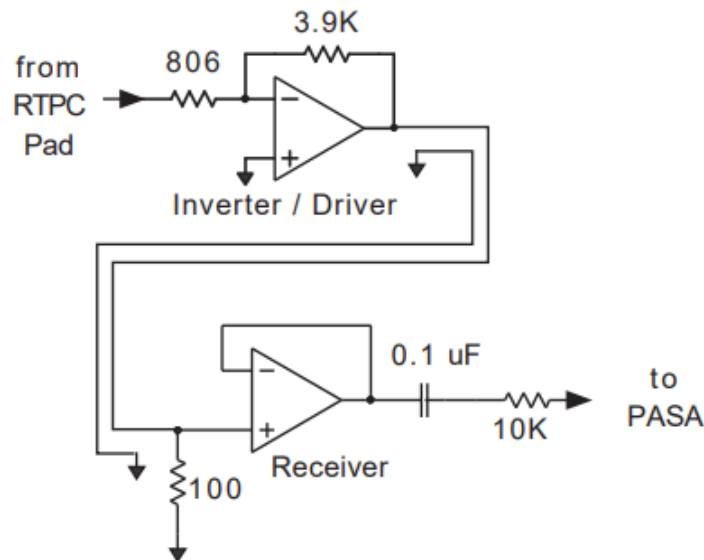
Figure 2.18: Schematic of a preamp and receiver

which shows the circuit that is attached to each channel [3].

Chapter 3

RTPC GAS MIXTURES

3.1 Gas Mixture Motivation

The focus of this chapter is to present the work that was done to identify the most effective gas mixture for use in Radial Time Projection Chamber (RTPC) that meets the needs for the Barely-Off-shell Nucleon Structure at 12 GeV (BONus12) experiment at Jefferson Lab. Ultimately, the goal of this experiment is to detect slow, backwards moving spectator protons from a deep inelastic collision of electron on neutrons in a deuteron target. These spectator protons will have a momentum of about 70-150 MeV/c and a direction above 100 degrees above the beamline [11]. This means that the gas mixture inside the RTPC must be at optimum conditions in order to minimize the energy threshold of the ionization electrons in the sensitive regions of the detector [11]. A small threshold reduces the constraints on the electronics and will yield a greater resolution. The ideal gas mixture also produce enough ionization electrons such that a distinction can be made between minimum ionizing particles from the spectator protons [11]. Where a minimum ionizing particle (mip) is a particle whose mean energy loss through a substance is close to the minimum. The goal of the gas simulations which will be discussed later in this chapter, is to determine the optimum gas mixture ratio and potential between the cathode and the readout pads in the RTPC which yield the fastest drift time along with the smallest drift angle.

3.2 Ideal Gas Mixtures
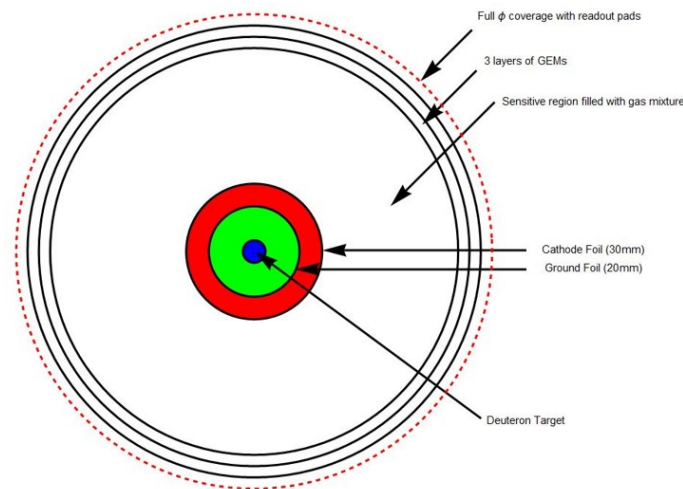
Figure 3.1: Diagram of the BONuS12 RTPC design as seen on the x-y plane. Constructed using Mathematica.

When charged particles traverse through a gas, the molecules and atoms that are inside the gas will become ionized. There are several factors that contribute to the amount of ionization that occurs. These factors include: the atomic number, density, and ionization potential of the gas [11]. The charge and energy of the incident particle will also dictate the number of ionization electrons that are produced.

The electrons that are created in this primary ionization process can create secondary ion-electron pairs, given that they have sufficient energy. Differing ionization rates of protons and lighter particles of the same momentum allow for easy discrimination between the protons and lighter particles. The properties of the gas or gas mixtures that yield these two processes for minimum ionizing particles can be quantified into the following: the number of primary electron-ion pairs per cm (N_p) and the sum of primary and secondary electron-ion pairs per cm (N_t) [11]. Another property that in useful to take into consideration is the excitation energy (E_x) and ionization energy (E_i), which is the amount of energy that is required to strip an electron from an atom. We will also examine the average energy that is required in order to create an electron-ion pair in the gas. This is denoted as (W_i).

Gas	Z	A	Density $\times 10^{-3}$ (g/cm^3)	E_x (eV)	E_i (eV)	W_i (eV)	$[dE/dx]_{mip}$	$N_p(cm^{-1})$	$N_p(cm^{-1})$
He	2	2	0.178	19.8	24.5	41	0.32	4.2	8
Ne	10	20.2	0.90	16.7	21.56	36.3	1.56	12	43
Ar	18	39.9	1.782	11.6	15.7	26	2.44	23	94
Xe	54	131.3	5.86	804	12.1	22	6.76	44	307
CF$_4$	42	88	3.93	12.5	15.9	54	7	51	100
DME	26	46	2.2	6.4	10.1	23.9	3.9	55	160
CO$_2$	22	44	1.98	5.2	13.7	33	3.01	33.5	91
CH$_4$	10	16	0.71	9.8	15.2	28	1.48	25	53
C$_2$H$_6$	18	30	1.34	8.7	11.7	27	1.15	41	111
iC$_4$H$_{10}$	34	58	2.59	6.5	10.6	23	5.93	84	195

Table 3.1: Properties of some gases and gas mixtures.

All of the numbers provided are for standard temperature 293 K and pressure 760 Torr. Where: N_p is the number of primary electron-ion pairs. N_i is the sum of primary and secondary electron-ion pairs. E_x is the excitation energy. E_i is the ionization energy. W_i is the average to create an electron-ion pair in the gas. $[dE/dx]_{mip}$ is the most probable energy loss by a minimum ionizing particle.[14]

Lastly, the most probable energy loss by a minimum ionizing particle will be considered, this is seen as $[dE/dx]_{mip}$ [11].

There are two specific reasons as to why an inelastic gas (gas mixture that is not solely made up of a noble gas) instead of a single gaseous environment is utilized. First, a primary gas must exist in which the primary ionization occurs. This gas must not interact with the walls of the detector and the probability that a drift electron is captured is low, thus it will have a low electron affinity. Given these parameters, the primary gas is usually chosen to be a noble gas such as helium, neon, or argon. The second gas in the mixture serves as a "quencher". The job of the second gas is to prevent secondary effects such as photon feedback and field emissions [11]. Which is a phenomenon in which charged particles are released from a material when it absorbs radiant energy. This gas will ensure that a stable mixture is achieved and is well separated from the background noise of the electronics [11]

Table 3.1 contains values for $(N_p), (N_t), (E_x), (E_i)$ along with other properties that are experimentally known for gases that could potentially be of use in the BONuS12 experiment [11] . Examining Table 3.1, we see that for the options for the primary gas (noble gases) the average energy that is re-

quired to create and electron-ion pair (W_i) is highest for He and lowest for Xe. At first glance, Xe might be considered as a viable candidate for our primary gas. However, when we examine the density of each gas, it can be concluded that although it would require more energy to create the electron-ion pair in He than in Xe, the particles will slow down significantly faster in Xe and could possibly never make it to the outer radius of the detector i.e. (the denser the gas, the faster the particles will slow down). Using He as the primary gas would ensure that the electrons would carry enough speed to make it to the outer radius of the RTPC and that they would also have a lower energy threshold detection [11]. This yields He as the best choice for the primary gas in our experiment. The next step is to determine which gas would be best served as the secondary or quencher gas. In the previous experiment BONuS6, dimethyl ether (DME) was used. DME is a colorless, highly flammable gas and is slightly toxic. It is worthy to note that in the previous experiment, the system failed just before production runs due to the fact that the exact ratio of He:DME was not held constant. This mixture was labeled as a "unknown parameter" in the final electron paths [3]. This caused 147,000 drift velocity vectors that needed to be determined and parameterized which caused strain in the readout electronics [3].

3.3 Drift Velocity, Drift Angle, and Diffusion

In order to optimize the gas mixture in the sensitive region of the RTPC (30cm to 70cm), the first aspect that must be considered is the drift velocity. Attaining a fast drift velocity will ensure that when the signals are received, they are unambiguous from other events occurring in the chamber such as Bremsstrahlung radiation which is braking radiation associated with acceleration during Coulomb collisions with nuclei [11]. The faster drift velocity will also be less demanding on the trigger and will yield less diffusion [11].

It is clear that the radial and azimuthal components of the electron drift paths are primarily sensitive to the drift gas mixture. This means that the next vital aspect that needs to be looked at is the minimization of the drift angle. In the scope of this thesis, the drift angle is in reference to the amount of azimuthal displacement in crossed electric and magnetic fields due to the Lorentz Angle [11]. These are the angles in which a particle moving in an electric field is deflected due to the effect of a magnetic field as seen in Fig 3.2. Minimizing the drift angle will essentially help to increase the resolution of the detector. The last property to be considered is the minimization of the diffusion that occurs inside the sensitive regions of the RTPC. Diffusion is the movement of an atom or molecule from a region of relatively high concentration to one of a lower concentration or in other words, the movement from high to low chemical potential. This gives rise to our needs for a gas mixture that yields a high drift velocity, small drift angles, minimum diffusion, and a high number of primary ionization events [11].

(a) Lorentz Angle vs Magnetic field
(b) Lorentz Angle vs Electric field
(c) v_ϕ vs Electric field
(d) v_r vs Electric field
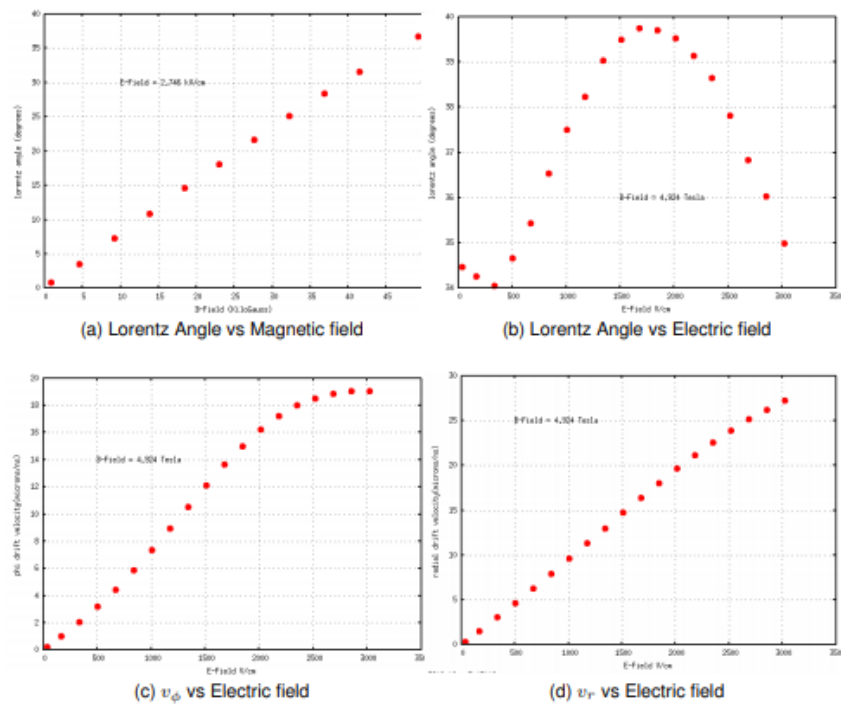
Figure 3.2: Simulated results using Magboltz showing in (a) and (b) the Lorentz angle's dependence on electric and magnetic fields in the RTPC. Shown in (c) and (d) are the radial and azimuthal components of the drift velocity dependence on the electric field with a constant magnetic field.

3.4 Garfield++ Simulation Analysis
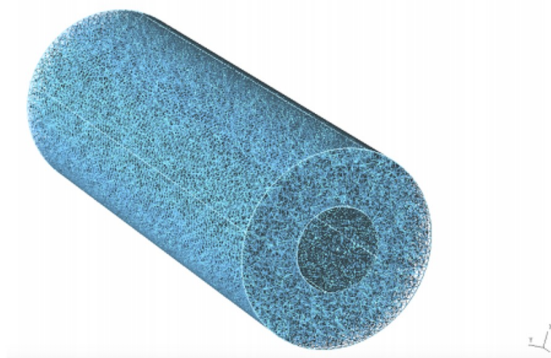
Figure 3.3: GMSH image of the RTPC for use with Garfield++

[11]

The program that was utilized to construct the gas mixture simulations was Garfield ++. Garfield ++ was developed at CERN [11]. This is an extended version of the original version that incorporates MagBoltz in the C++ lan-

guage [11].

MagBoltz is used to solve the Boltzman transport equations for electrons in a gas mixture under the influence of electric and magnetic fields. This software is a tool kit for the simulation of detectors with gases as sensitive mediums [3]. Garfield++ has several aspects that are advantages to the BONuS12 experiment. These advantages include: verification of cluster yield and energy deposited in the simulations, the results are extremely sensitive to electric and magnetic fields which provides a more realistic outcome, and the results that are given can be compared with any other data. Other software that was also used by Nathan Dzbenski to create a mesh of the RTPC and solve the electromagnetic equations inside the RTPC are GMSH [11] and ElmerSolver [3][11]. Fig 3.3 represents the mesh of the RTPC that was imported into Garfieldd++ in order to conduct the simulations. The potential that ElmerSolver uses to calculate the electric field inside the RTPC is seen in Fig 3.4 beginning with 3500 V on the cathode [11]. The code that was used in the simulations is seen in Fig.A2 in the Appendix. Fig 3.2 demonstrates an example how the drift velocity and Lorentz angle components change with the electric and magnetic fields that are present in the RTPC.

3.5   Results-Quencher Ratios

Since He has been chosen as the primary gas, the next step is to determine the quencher gas that will be used inside the RTPC. Fig 3.4 shows the drift time as a function of the drift angle of four gas mixtures in a sensitive region containing a potential of 2500 V with radii from 6 cm to 8 cm. The initial and final radii were chosen to gather results quickly. The error bars on these points represent the diffusion properties of the mixture. This data was obtained and plotted by Nathan Dzbenski [11].   From Fig 3.4 it can be seen that the ratios of He-Isobutane HC(CH3)3 all result in seemingly identical values for drift angle and drift time. The ratio of He:DME starts at 85:15 on the left of Fig 3.4 and goes to 100:0 on the right. At a ratio of 87:15 He:DME is at the minimum of the curve. This ratio could be chosen for this experiment as it was in the BONuS6 experiment, however, to meet our needs, it would be preferable to chose a quencher gas that is non-flammable. Given this parameter, we chose to examine the properties of a $He : CO_2$ mixture.
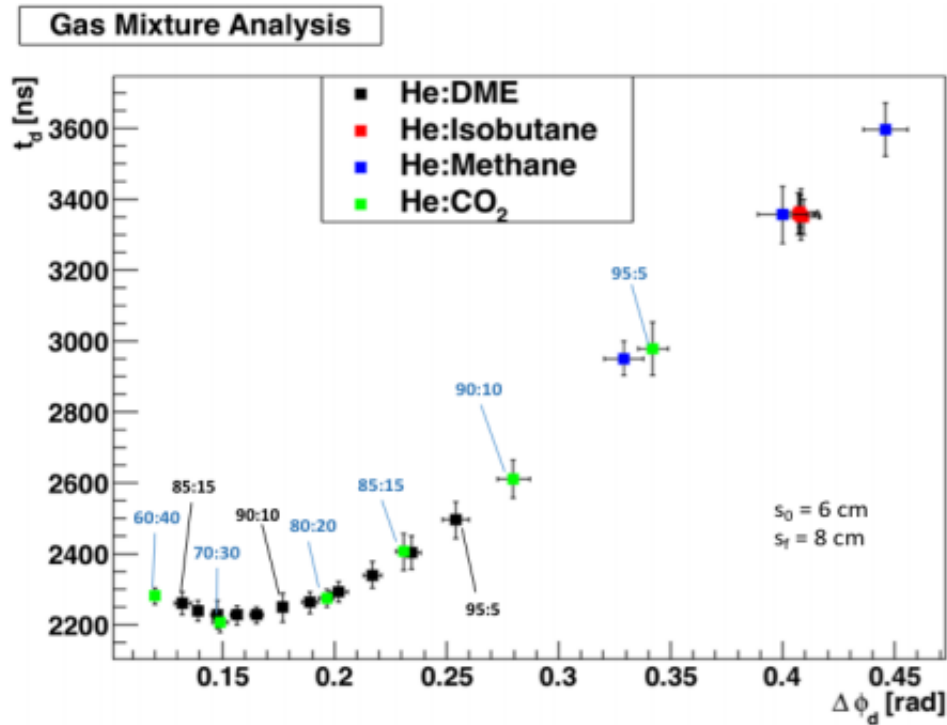
Figure 3.4: Plot of drift time (t_d) as a function of drift angle $(\delta\phi_d)$ with a potential difference of 2500 V across the drift region[11]

The $He : CO_2$ as seen in Fig 3.4 is labeled in green with the ratios labeled in blue [11]. We see that the 70:30 mixture ratio is located at the minimum of the data so this meets our standards. Another aspect of the mixture that needs addressing are the locations where slight changes in the mixture would occur. If we chose the minimum location on the graph, detecting where these slight changes may occur can prove to be problematic. Even though there are changes in the drift angle as the ratio changes, at the minimum location the variations in the drift time are on the order of nanoseconds rendering them virtually imperceptible during experimental runs. If another ratio was considered, say 80:20 $He : CO_2$, then we could easily identify if a change occurs during an experimental run by the noticeable change in both the drift angle and drift time [11]. For this reason, as well as its non-flammability, we will explore the data range for the $He : CO_2$ ratios for which my simulations occurred was from 77.0:23.0 to 83.0:17.0 in 0.1 increments with each run taking approximately 3 hours to compile.At the end of each gas mixture simulation of 500 events per ratio, Graphs for

the drift time, Lorentz Angle, Drift velocity, and potential were formulated by Garfield++. The factors that were held at a constant value for the simulations can be seen in Table 3.5 An example of the graphs that were formulated for the 80:20 $He : CO_2$ mixture can be seen in Fig 2.6. Table 2.3 in the Appendix shows the results of the simulations that were obtained using Jefferson Lab ifarm and Garfield++.
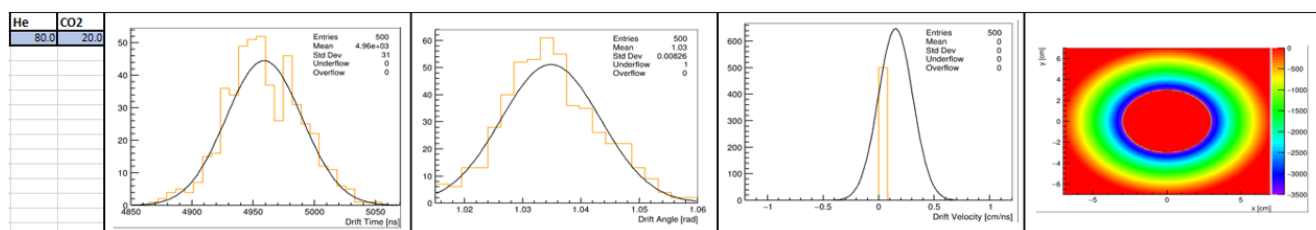
Figure 3.5: Plots generated by Garfield++ for 80:20 $He : CO_2$ gas mixture ratio.

Since we have chosen the primary gas to be He and and quencher gas to be CO_2, we will examine the range of these ratios as discussed earlier. In Fig 3.6 and Fig 3.8, we have a graph of drift time as a function of Lorentz angle (drift angle). Upon examination, it is seen that gas mixtures with $He : CO_2$ ratio of 77.6:22.4 has the lowest drift angle. However,if this mixture is used, it might show that small changes might have minute timing differences that could be missed during an experimental run. Given this, gas mixture ratios between 78.5:21.5 to 80:20 might want to be considered for experimental conditions. It can be seen that using Microsoft Excel to plot the range of $He : CO_2$ gas mixture ratios that the fit will be a polynomial which has the form as seen in Eq 3.1.

$$y = 2160.8x^2 - 3413.3x + 6178.7. \tag{3.1}$$

It can be seen in Fig 3.8 that the $He : CO_2$ mixture of 79.5:20.5 has one of the lowest diffusion value. Thus, this could potentially be a gas mixture ratio that could potentially be used in an experimental run. This figure can also be used to eliminate outliers in gas mixture ratios. Fig 3.7 could also be used eliminate outliers in gas mixture ratios.
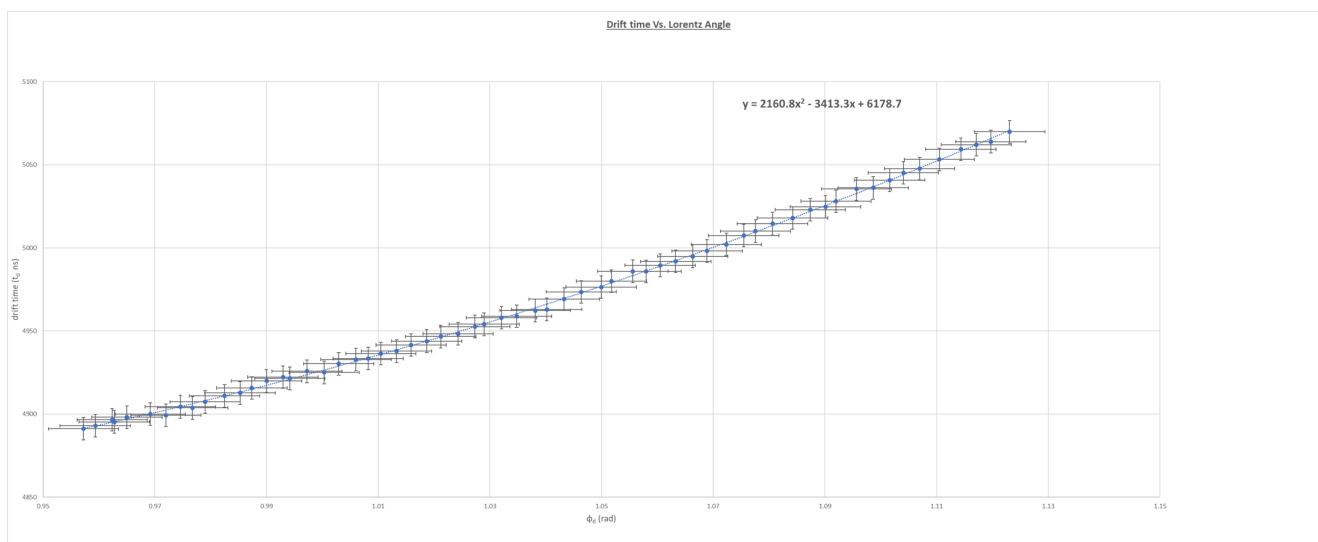
Figure 3.6: Plots generated by Excel for $He : CO_2$ gas mixture ratios. Drift time as a function of drift angle.
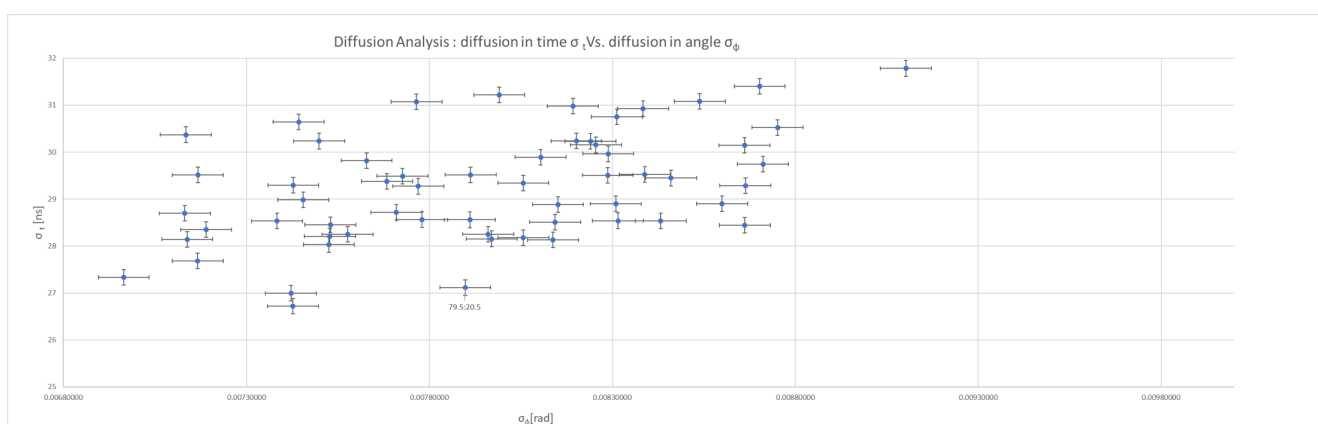
Figure 3.7: Plots generated by Excel for $He : CO_2$ gas mixture ratios.

Temperature(K)	Pressure(Torr)	Magnetic Field	Electric Field	Potential (V)	En
293	760	B_x=0 B_y=0 B_z=5 T	E_x=875 E_y=0 E_z=0	-3500	36

Table 3.2: Constants used for Simulation

With these parameters implemented, the ratio of the gas mixtures were changed fairly easy that in turn yielded experimentally verified results. Utilization of Garfield++ yields analysis of the gas mixture ratios without the need to purchase many combinations of gas canisters and removes the need to experimentally test every mixture [11].

Drift Time VS. Lorentz Angle
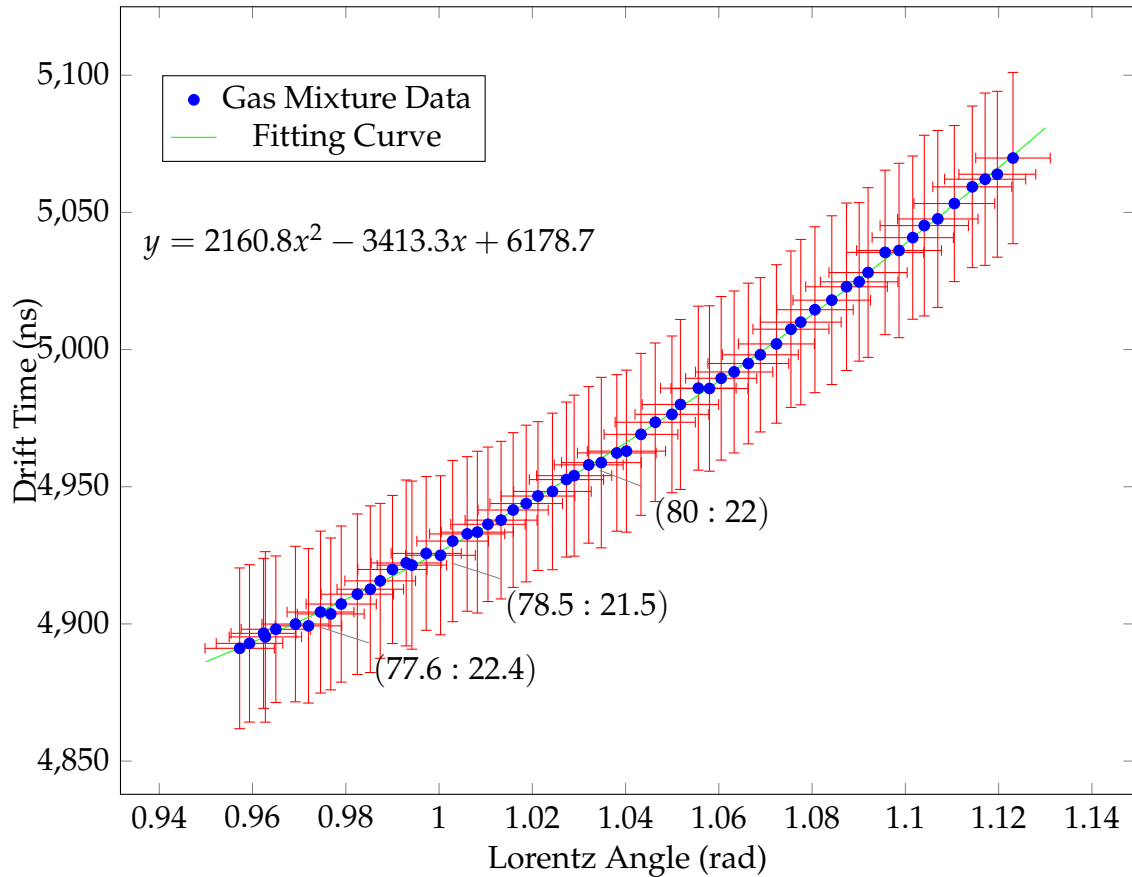
Figure 3.8: Plot of drift time (t_d) as a function of drift angle ($\Delta\phi_d$) with a potential difference of 3500 V across the drift region.

3.6 Error Analysis

There are several systematic errors that must be accounted for. The first source of error is variations in the magnetic field. The field generated by the soleniod magnet will not be uniform as was assumed in the garfield ++ simulations. Garfield ++ was modified in order to load a magnetic field map in order to study the effects of variations from our current field map. It can be seen that as electrons are created closer to the edges of the RTPC, we get closer to a 2 percent change in drift time and drift angle. This change must be accounted for systematically. Another source of systematic errors are the signals on the electronics. As electrons hit the readout pads, they accumulate and create a readable signal for our electronics. This accumulation is represented by a distribution of energy deposited on that readout
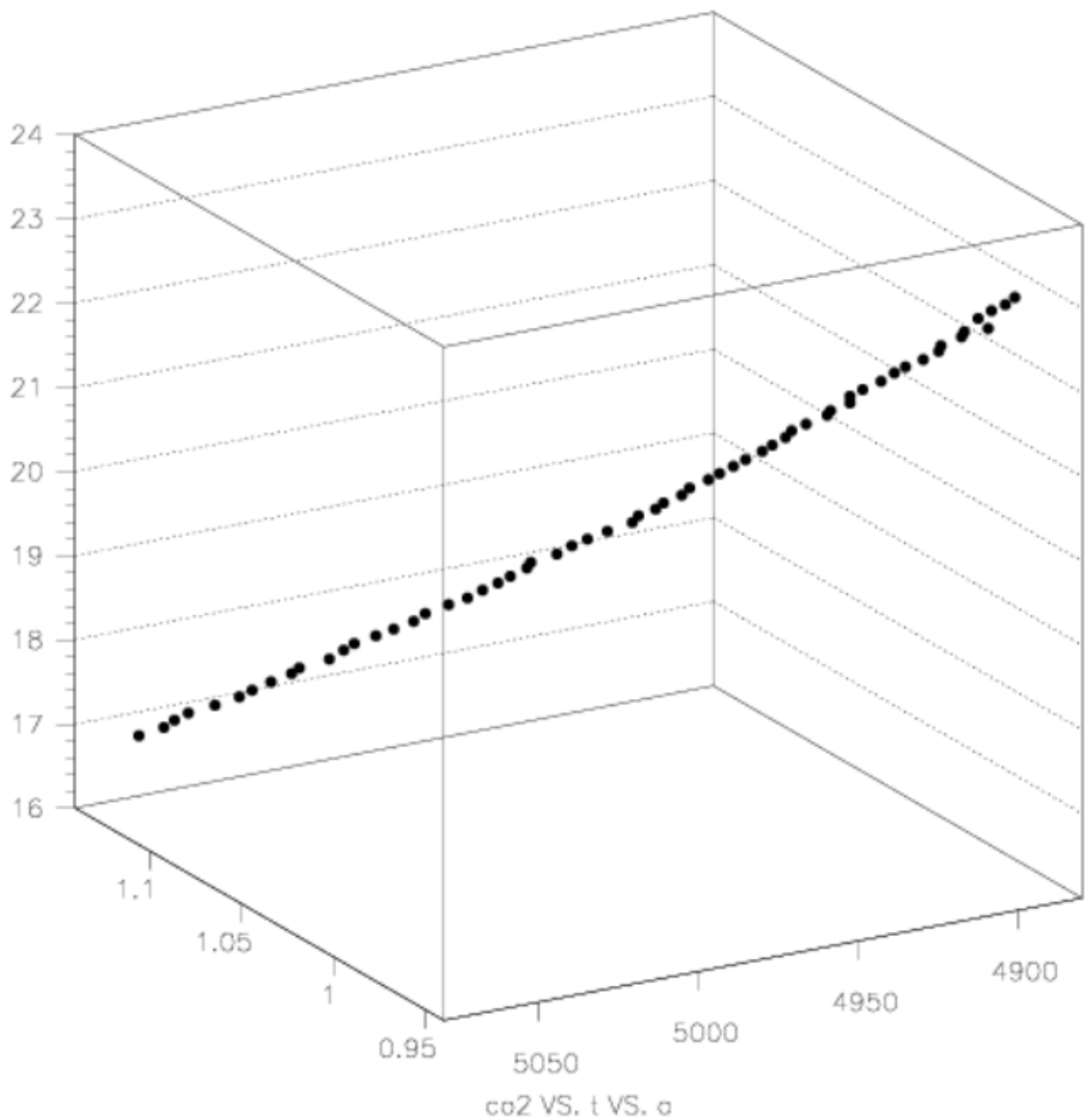
Figure 3.9: Plots generated by Excel for $He : CO_2$ gas mixture ratios.

pad. The accumulations will have a mean and standard deviation that is an systematic error associated with that signal.

There will also exist alignment issues that produce systematic error. When the RTPC is installed into CLAS 12. It is vital that this is done with high precision. However, it is almost impossible to ensure that the x=0,y=0, and
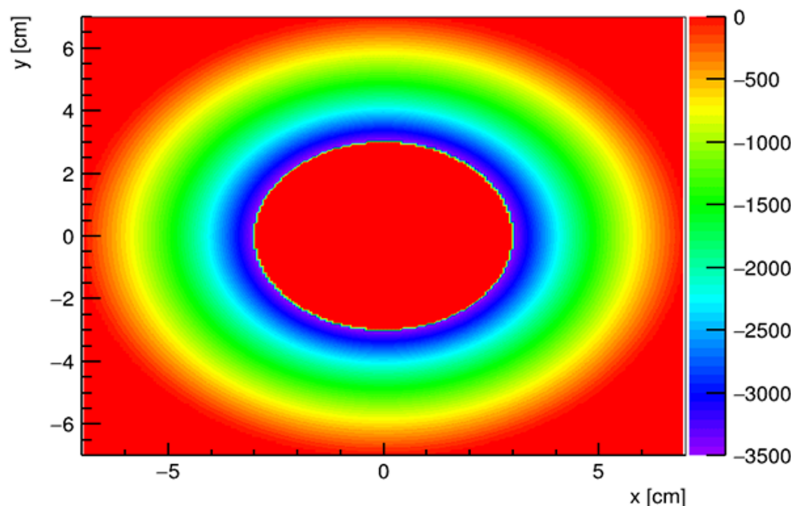
Figure 3.10: Garfield++ representation of the potential inside the RTPC, with 3500 V on the cathode

[11] This was taken from one of the many potential graphs from the simulations.

z=0 position. Even the slightest offset in any direction will mean that event reconstruction will deviate. Another source of error that could potentially be introduced is the fitting curve used by Microsoft Excel to extract Eq 2.1. Also, due to the cylindrical geometry of the cathode, the foil may be wrinkled or contain external contaminates (i.e. fingerprints/oils) that would have an impact on the potential that can safely exist across the RTPC [11].

Appendix A

```cpp
//_____
//_____Variables_____
//_____

 // Magnetic field
 const double Bx = 0.; // Tesla
 const double By = 0.; // Tesla
 const double Bz = 5.; // Tesla

 // Electric Field [V/cm]
    const double Ex = 875.;
    const double Ey = 0.;
    const double Ez = 0.;

    // Drift velocity variables
    Double_t vx, vy, vz;

 // Set the initial position [cm] and starting time [ns].
 double x0 = 3.001, y0 = 0.0, z0 = 10.0, t0 = 0.;
 // Set the initial energy [eV].
 double e0 = 1;
 // Set the initial direction (x, y, z).
 // In case of a null vector, the direction is randomized.
 double dx0 = 0., dy0 = 0., dz0 = 0.;
 // Calculate an electron avalanche
 int ne, ni;
 int ne_tot;
 // Electron information after the avalanche
 Double_t x1, y1, z1, t1,e1;
 Int_t status;

//_____
//_____ Canvas and plots _____
//_____

 TCanvas * c_field = new TCanvas("c_field", "c_field", 800, 600);
 TCanvas *c_driftT = new TCanvas("c_driftT","Drift time",800,600);
 TCanvas *c_energy = new TCanvas("c_energy","Energy Loss",800,600);
 TCanvas *c_driftV = new TCanvas("c_driftV","Drift Velocity",800,600);
 TCanvas *c_phi = new TCanvas("c_phi","Lorentz angle",800,600);

 ViewField *viewfield = new ViewField();

   TH1D *h_driftT = new TH1D("h_driftT","Drit Time 2500 V (He_80_CO2_20)",30,0,0);
   TH1D *h_energy = new TH1D("h_energy","Energy Loss 2500 V (He_80_CO2_20)",30,0,0);
   TH1D *h_driftV = new TH1D("h_driftV","Drift Velocity",30, 0, 0);
   TH1D *h_phi = new TH1D("h_phi","Lorentz angle 2500 V (He_80_CO2_20)",20,0,0);

 TF1 *gausfit = new TF1("gausfit","gaus",0,8000);

//_____
//_____ Openings _____
//_____

 // Setup the gas.
 MediumMagboltz* gas = new MediumMagboltz();
// gas->LoadGasFile("gasFiles/He_100_DME_00.gas");
 gas->SetComposition("He",83.0,"CO2",17.0);
 gas->SetTemperature(293.);
 gas->SetPressure(760.);

   gas->EnableDrift();                              // Allow for drifting in this medium
 gas->PrintGas();

 // Import an Elmer-created LEM and the weighting field for the readout electrode.
 ComponentElmer * elm = new ComponentElmer("RTPC/mesh.header","RTPC/mesh.elements","RTPC/mesh.nodes",
 "RTPC/dielectrics.dat","RTPC/RTPC.result","cm");
 elm->SetMedium(0,gas);
 elm->SetMagneticField(Bx,By,Bz);
```

```cpp
// Assemble a Sensor object
Sensor* sensor = new Sensor();
sensor->SetArea(-7.0,-7.0,-20.0,7.0,7.0,20.0);
// Calculate the electric field using the Component object cmp
sensor->AddComponent(elm);

TCanvas *c_e = new TCanvas("Cell","Cell");
ViewDrift* v_e = new ViewDrift();
v_e->SetCanvas(c_e);
v_e->SetArea(-7.0,-7.0,-20.0,7.0,7.0,20.0);


// Evaluate the number of electrons in the avalanche
AvalancheMicroscopic* aval = new AvalancheMicroscopic(); // did not get it to work with AvalancheMC()
//AvalancheMC* aval = new AvalancheMC();
  aval->SetSensor(sensor);
aval->EnablePlotting(v_e);
aval->EnableMagneticField();



for(int eve=0;eve<500;eve++){
  ne_tot=0;
  cout << "Event number: " << eve << endl;
  aval->AvalancheElectron(x0, y0, z0, t0, e0, dx0, dy0, dz0);

  // Get the number of electrons and ions in the avalanche.
  aval->GetAvalancheSize(ne, ni);
  ne_tot+=ne;

  if(0<aval->GetNumberOfElectronEndpoints()){
    for(int nava=0;nava<aval->GetNumberOfElectronEndpoints();nava++){
      aval->GetElectronEndpoint(nava, x0, y0, z0, t0, e0, x1, y1, z1, t1, e1, status);

      gas->ElectronVelocity(Ex, Ey, Ez, Bx, By, Bz, vx, vy, vz);

      h_driftV->Fill(vx);
      h_driftT->Fill(t1);
      h_energy->Fill(e0-e1);
      if(x1>0 || x1<0) h_phi->Fill(TMath::ATan(y1/x1));
    }
  }
  //if(0<ne_tot) h_size->Fill(ne_tot);
//    v_e->Plot();
}
```

```
//_____
//_____ Display _____
//_____

  viewfield->SetComponent(elm);
  viewfield->SetSensor(sensor);
  viewfield->SetCanvas((TCanvas*)c_field->cd());
  viewfield->SetWeightingFieldRange(0.0, 10000.0);

//  Field plot
  c_field->cd();
  viewfield->PlotContour();

  c_driftV->cd();
   h_driftV->Draw();
   h_driftV->Fit("gausfit","Q");
   h_driftV->GetXaxis()->SetTitle("Drift Velocity [cm/ns]");

  c_driftT->cd();
   h_driftT->Draw();
   h_driftT->Fit("gausfit","Q");
cout << "Drift time" << endl;
cout << "Mean = " << gausfit->GetParameter(1) << ", Sigma = " << gausfit->GetParameter(2) << endl;
   h_driftT->GetXaxis()->SetTitle("Drift Time [ns]");

  c_phi->cd();
   h_phi->Draw();
   h_phi->Fit("gausfit","Q");
cout << "Lorentz angle" << endl;
cout << "Mean = " << gausfit->GetParameter(1) << ", Sigma = " << gausfit->GetParameter(2) << endl;
   h_phi->GetXaxis()->SetTitle("Drift Angle [rad]");

  //c_pos->cd();
  //  h_pos->Draw();


  app.Run(kTRUE);
```

Gas Mixture		# Events	Drift Time		Lorentz angle	
He	CO2		mean	sigma	mean	sigma
77.0	23.0	500	4891.11	29.2952	0.957241	0.00742813
77.1	22.9	500	4892.91	28.697	0.959351	0.0071319
77.2	22.8	500	4895.27	31.0713	0.962755	0.0077649
77.3	22.7	500	4898.06	26.719	0.965004	0.0074272
77.4	22.6	500	4896.56	27.336	0.96236	0.0069647
77.5	22.5	500	4899.95	28.3476	0.969203	0.0071901
77.6	22.4	500	4899.3	28.1423	0.972001	0.0071384
77.7	22.3	500	4904.32	29.5121	0.97458	0.0071676
77.8	22.2	500	4903.64	27.6809	0.976769	0.0071667
77.9	22.1	500	4907.24	28.4525	0.979019	0.0075297
78.0	22.0	500	4910.83	29.2717	0.98248	0.0077696
78.1	21.9	500	4912.65	30.3699	0.985259	0.0071347
78.2	21.8	500	4915.69	28.2478	0.987385	0.0075769
78.3	21.7	500	4919.84	26.993	0.990016	0.0074219
78.4	21.6	500	4922.22	30.2335	0.992953	0.0074989
78.5	21.5	500	4921.43	30.6426	0.994183	0.007443
78.6	21.4	500	4925.7	28.0304	0.99724	0.0075253
78.7	21.3	500	4925.02	28.9844	1.00032	0.0074555
78.8	21.2	500	4930.2	29.3785	1.00292	0.0076842
78.9	21.1	500	4932.8	28.1776	1.00603	0.0080568
79.0	21.0	500	4933.45	29.4892	1.00822	0.0077269
79.1	20.9	500	4936.31	28.1539	1.01049	0.0079704
79.2	20.8	500	4937.83	28.7175	1.0133	0.0077099
79.3	20.7	500	4941.52	28.2083	1.01589	0.0075279
79.4	20.6	500	4943.88	28.5593	1.01869	0.0077804

79.5	20.5	500	4946.61	27.1178	1.02121	0.0078983
79.6	20.4	500	4948.29	28.5382	1.02432	0.0083155
79.7	20.3	500	4952.61	28.2538	1.02732	0.0079609
79.8	20.2	500	4954.04	29.3437	1.02897	0.0080565
79.9	20.1	500	4957.97	28.5309	1.03209	0.007384
80.0	20.0	500	4958.8	31.0809	1.0348	0.0085388
80.1	19.9	500	4962.32	28.5329	1.03812	0.0084324
80.2	19.8	500	4962.98	29.524	1.04018	0.008389
80.3	19.7	500	4969.09	29.5174	1.0433	0.0079126
80.4	19.6	500	4973.5	28.8992	1.04636	0.0086
80.5	19.5	500	4976.39	28.5573	1.04994	0.007911
80.6	19.4	500	4979.99	30.9773	1.05176	0.0081925
80.7	19.3	500	4985.93	29.8933	1.0556	0.0081044
80.8	19.2	500	4985.81	30.1509	1.05799	0.0082553
80.9	19.1	500	4989.53	29.8196	1.0605	0.0076287
81.0	19.0	500	4991.84	29.5075	1.06328	0.0082876
81.1	18.9	500	4994.92	29.2883	1.06632	0.008664
81.2	18.8	500	4998.1	28.1282	1.0689	0.0081379
81.3	18.7	500	5002.05	28.8849	1.07235	0.0081518
81.4	18.6	500	5007.43	28.5103	1.07546	0.0081436
81.5	18.5	500	5010	30.1424	1.07757	0.0086614
81.6	18.4	500	5014.53	30.2358	1.08061	0.008202
81.7	18.3	500	5018.01	30.7489	1.08422	0.0083126
81.8	18.2	500	5022.89	30.5235	1.08738	0.0087517
81.9	18.1	500	5024.69	28.8987	1.09009	0.0083096
82.0	18.0	500	5028.08	30.926	1.092	0.0083842
82.1	17.9	500	5035.41	29.9651	1.09565	0.0082888

82.2	17.8	500	5036.12	31.7816	1.09864	0.0091025
82.3	17.7	500	5040.8	29.7441	1.10158	0.0087119
82.4	17.6	500	5045.19	32.939	1.10405	0.0094734
82.5	17.5	500	5047.62	32.2451	1.10695	0.0086272
82.6	17.4	500	5053.23	28.4414	1.1105	0.0086619
82.7	17.3	500	5059.32	29.446	1.11435	0.0084605
82.8	17.2	500	5062.1	31.4007	1.1171	0.0087029
82.9	17.1	500	5063.91	30.2279	1.11972	0.0082402
83.0	17.0	500	5069.81	31.2182	1.12308	0.007991

TABLE A.1: Results from Garfield++

BIBLIOGRAPHY

[1] https://www.jlab.org/12GeV, Hall B Wiki, Aug 25,2016.

[2] Zhang. Jixie,Ph.D. thesis, Old Dominion University (2010)

[3] Baillie. N,Ph.D. thesis, William and Mary (2009)

[4] https://science.energy.gov/np/facilities/user-facilities/cebaf/,Department of Energy (2017)

[5] 12 Gev Upgrade, Design Solutions Document Upgrade to Hall B, Jefferson Lab, Department of Energy,(2010)

[6] Superconducting Magnets, Jefferson Lab, Daniel S. Carman,(2013).

[7] Hall B Superconducting Magnets for the CLAS12 detector at JLAB, Jefferson Lab, I. Quettier,(2010).

[8] Forward Time-of-Flight Geometry for CLAS12, Jefferson Lab, Daniel S. Carman,(2016).

[9] M. Mestayer et al., Nucl. Instr. Meth. A449, 81 (2000).

[10] E. Smith et al., "The time-of-flight system for CLAS," Nuclear Instruments and Methods in Physics Research A, vol. 432, pp. 265–298, 1999.

[11] Gas Mixture Analysis for BoNuS12 RTPC, Nathan Dzbenski, Old Dominion University, July(2017).

[12] S. Tkachenko et al. Phys. Rev. C89 (2014) 045206.

[13] P.R. Burchat, etc. Studies of Helium Gas Mixtures in Drift Chambers. SLAC-PUB-5626 (1991).

[14] A. Sharma. Properties of some gas mixtures used in tracking detectors http://www.slac.stanford.edu/pubs/icfa/summer98/paper3/paper3.pdf

[15] Y. Assran, etc. Transport Properties of operational gas mixtures used at LHC. https://arxiv.org/pdf/1110.6761

[16] Garfield++, http://garfieldpp.web.cern.ch/garfieldpp/

[17] C. Geuzaine, J.F. Remacle http://gmsh.info

[18] Elmer.https://www.csc.fi/web/elmer

[19] The Structure of the Free Neutron at Large x-Bjorken, A 12 GeV Research Proposal to Jefferson Lab,S. Bultmann, G.E. Dodge, C.E. Hyde Old Dominion University, 2008.

[20] F. Sauli. A New Concept for Electron Amplification In Gas Detectors, MethodsNuclear Instruments and Methods in Physics Research A. 386.Nov. 1996.

[21] L.Musa, et al.,Proc. of IEEE Nuclear Science Symposium 2003, Portland, USA (2003).

[22] S. Tkachenko, N. Baillie, S.E. Kuhn, Phys. Rev. C 89, 045206 (2014).